

JGR Solid Earth

RESEARCH ARTICLE

10.1029/2018JB017289

Key Points:

- We calculate deviatoric stresses associated with GPE variations coupled with mantle tractions in Indian plate and IN-EU collision zone
- We evaluate various tomography models by comparing the predicted parameters of stress, strain, and velocities against observations
- The regional model of Singh et al. (2014) embedded within the global model of S4ORTS provides the best fit to surface observables

Correspondence to:

S. Singh,
srishtis@iisc.ac.in

Citation:

Singh, S., & Ghosh, A. (2019). Surface motions and continental deformation in the Indian plate and the India-Eurasia collision zone. *Journal of Geophysical Research: Solid Earth*, 124. <https://doi.org/10.1029/2018JB017289>

Received 31 DEC 2018

Accepted 19 AUG 2019

Accepted article online 21 AUG 2019

Surface Motions and Continental Deformation in the Indian Plate and the India-Eurasia Collision Zone

Srishti Singh¹  and Attreyee Ghosh¹ 

¹Centre for Earth Sciences, Indian Institute of Science, Bangalore, India

Abstract The collision of the Indian plate with Eurasia has played a major role in controlling the dynamics of central Asia leading to the world's largest continental deformation zone. In order to study the deformation within the Indian plate as well as the India-Eurasia collision zone, we model the lithospheric stress field by calculating the two primary sources of stress, one arising due to topography and shallow lithospheric structure estimated by gravitational potential energy differences and the other arising from basal tractions derived from density-driven mantle convection. We use several tomography models to calculate horizontal tractions using the convection code HC for two radially varying viscosity structures. We also take into account lateral viscosity variations in the lithosphere model arising from stiff cratons, weak plate boundaries, and strength variations due to old and young oceanic lithosphere. We do a quantitative comparison of our predicted deviatoric stresses, strain rates, and plate velocities with surface observables and find that the regional tomography model of Singh et al. (2014) embedded in the global *S* wave model S4ORTS does a remarkable job of fitting the observations of GPS velocities and strain rates as well as intraplate stress field from the World Stress Map.

1. Introduction

The India-Eurasia collision zone is one of the largest areas of continental deformation in the world (Figure 1). The ongoing collision between the Indian and the Eurasian plates is a major factor in controlling the present-day dynamics of the Indian plate (Banerjee et al., 2008; Molnar & Tapponnier, 1975; Molnar & Stock, 2009; Molnar et al., 1993; Patriat & Achache, 1984), though some studies have suggested the Réunion plume to be an important contributor to plate motion changes for the Indian plate (Cande & Stegman, 2011; Morgan, 1972; van Hinsbergen et al., 2011). The Indian plate is surrounded by some of the most active plate boundaries (DeMets et al., 1990; Khattri & Tyagi, 1983; Lawrence et al., 1981; Molnar et al., 1973; Molnar & Tapponnier, 1975). The Chaman transform zone, comprising major strike slip faults such as Chaman, Gardez, West and East Waziristan, Sulaiman, Ghazaband, and Ornach-Nal faults, connects the Makran and Himalayan convergence zones and marks the western boundary of the Indian plate with Eurasia (Lawrence et al., 1981). The Makran subduction zone is a convergent boundary between the Arabian and the Eurasian plates. In the north, the Indian plate is bounded by ~2,500-km-long Himalayan Mountain Belt where the Main Frontal Thrust marks the boundary of the southern margin of the Himalayan collision zone. There occurs a syntactical bend in the plate boundary toward the east, known as the Eastern Himalayan Syntaxis (EHS), which extends into the Indo-Burmese Range (IBR) that separates the Indian plate from Burma (Figure 1). Further south, this boundary transitions into the Andaman Sumatra subduction zone (ASSZ), which is an oblique ocean-continent subduction boundary. The Indo-Australian plate (IAP) boundary, which marks the southern boundary of the plate, is more of a diffuse plate boundary rather than an active one. In the southwest, the Indian plate is separated from the African plate by the Carlsberg Ridge, which is the northern segment of the Central Indian Ridge.

The presence of the collisional boundary in the north makes northern India a region of high seismic hazard (Bhatia et al., 1999; Khattri et al., 1984; Parvez et al., 2003). A better understanding of the deformation in this region would help in seismic hazard assessment. Numerous studies have investigated the deformation in this region using GPS (Bilham et al., 1997; Chen et al., 2000; Holt, 2000; Larson et al., 1999; Paul et al., 2001; Shen et al., 2005; Zhang et al., 2004, 2017), interferometric synthetic aperture radar (Huang et al., 2014; Ryder et al., 2007), field and radiometric data (Ratschbacher et al., 1994), and earthquake focal mechanisms (Biswas, 1989; Holt et al., 1991, 1995; Molnar & Tapponnier, 1978; Ni & Barazangi, 1985; Tapponnier & Molnar, 1979). These studies have suggested the Himalayan front to be predominantly

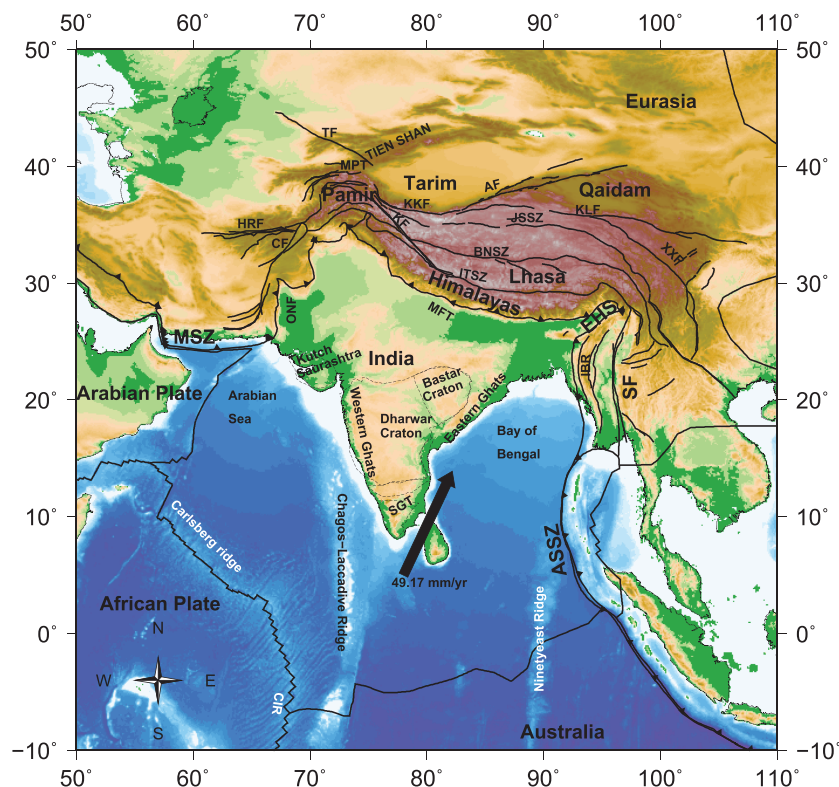


Figure 1. The Indian plate and India-Eurasia collision zone. Black arrow indicates motion of the Indian plate with respect to a fixed Eurasia (Kreemer et al., 2014). Abbreviations: AF = Altyn Tagh fault; CF = Chaman Fault; HRF = Herat Fault; KF = Karakorum Fault; KKF = Karakax Fault; KLF = Kunlun Fault; MFT = Main Frontal Thrust; MPT = Main Pamir Thrust; ONF = Ornach-Nal Fault; EHS = Eastern Himalayan Syntaxis; SF = Sagaing Fault; TF = Talas-Fergana Fault; XXF = Xianshuixi-Xiaojiang Fault system; MSZ = Makran Subduction Zone; IBR = Indo-Burmese Ranges; ITSZ = Indus-Tsangpo Suture Zone; BNSZ = Bangong-Nujiang Suture Zone; JSSZ = Jinshajiang Suture Zone; ASSZ = Andaman Sumatra subduction zone; CIR = Central Indian Ridge; SGT = Southern Granulite Terrane.

defined by thrust mechanism that transitions to strike-slip system in the north and the east. Holt et al. (1991), Molnar and Tapponnier (1975), Shen et al. (2005), and others predicted strike-slip mechanism as the dominant mode of faulting for several roughly E-W trending faults in the northeast of Himalayan chain or southeast borderland of Tibetan plateau and east of EHS. The deformation within the Indian peninsula has been suggested to be minor. Paul et al. (2001) obtained no significant strain larger than 7×10^{-9} year $^{-1}$ across India using GPS measurements.

The collision of the Indian plate with Eurasia led to the rearrangement of plate boundaries in the Indian Ocean along with dramatic changes in plate motions (Copley et al., 2010; Liu et al., 1983; Patriat & Achache, 1984). This ongoing collision since ~ 50 Ma caused a decrease in the rate of convergence (Molnar & Tapponnier, 1975; Patriat & Achache, 1984). Iaffaldano et al. (2013), Merkouriev and DeMets (2006), Molnar and Stock (2009), and others agreed on a slowdown in convergence, at least between 20 and 10 Ma. Curran and Munasinghe (1989), Iaffaldano et al. (2006), Molnar et al. (1993), and Weissel et al. (1980) have linked the deformation within the IAP, especially in the eastern and central Indian Ocean, to the rise of the Tibetan Plateau. However, Ghosh et al. (2006) argued that the Tibetan uplift could not be the sole cause of the deformation in the Indian Ocean, by calculating the deviatoric stresses associated with gravitational potential energy (GPE) differences between the elevated ridges, the deeper Indian Ocean, and the Tibetan Plateau. They found these GPE-related deviatoric stresses to be much lower than those of Molnar et al. (1993) and insufficient to cause the deformation of the Indian Ocean region. Iaffaldano et al. (2018) attributed the deformation in the central Indian ocean to the Capricorn plate motion changes driven by eastward asthenospheric flow, associated with the Réunion plume.

The plate tectonic theory has been very useful in understanding the deformation process, especially within oceanic plates where deformation is mostly confined to narrow zones (Morgan, 1968; Wilson, 1965). But continental deformation has proven to be more complex as it is more diffuse in nature, thus suggesting a significant departure from one of the basic assumptions of plate tectonics, that deformation is confined along narrow plate boundaries (Wilson, 1965). There have been two approaches to continental kinematics; one that treats the lithosphere as comprising of rigid plates/blocks, emphasizing deformation on major faults and neglecting the minor deformation occurring aseismically or on smaller faults (Avouac & Tapponnier, 1993; Matte et al., 1996; Peltzer & Tapponnier, 1988; Peltzer & Saucier, 1996; Tapponnier et al., 1982); the other considers deformation as continuous, yet heterogeneous and driven by varying crustal thickness (England & Houseman, 1989; England & McKenzie, 1982; 1983; England & Molnar, 1997; Flesch et al., 2001, 2007; Ghosh et al., 2006, 2008, 2009, 2013, 2019; Hirschberg et al., 2018; Husson & Ricard, 2004; Zhang et al., 2004). One can find observations that both support as well as disprove the block model (see ; Calais et al., 2006). Flesch et al. (2001) showed that GPE differences have major contribution in deciding the spatially varying style and magnitude of strain rates around the Tibetan Plateau, by using thin viscous sheet model that considers deformation as continuous. England and Molnar (2005) argued that block-like motion is valid for Tarim, south China, and the Amurian region, while continuous deformation dominates the rest of Asia. The varying crustal thickness leads to lateral variations in GPE that contribute to the forces driving deformation (England & Houseman, 1986; Frank, 1972; Houseman & England, 1986, 1993; Molnar & Tapponnier, 1978). In the case of continental areas, the horizontal dimensions of deformation far exceed the thickness of the lithosphere; thus, various studies have used thin sheet models to constrain the deformation resulting due to these buoyancy forces (Calais et al., 2006; England & McKenzie, 1982, 1983; England & Houseman, 1989; England & Molnar, 1997; Flesch et al., 2001, 2007; Flesch & Kreemer, 2010; Ghosh et al., 2006, 2008, 2009, 2013, 2019; Hirschberg et al., 2018; Husson & Ricard, 2004; Iaffaldano et al., 2006; Kong & Bird, 1995; Richardson et al., 1979; Sandiford & Coblenz, 1994; Vergnolle et al., 2007; Zhang et al., 2004). Thin sheet approximation is based on the assumption that the gradients of shear tractions at the base of the plate are negligibly small compared to the force of gravity acting on density. Both approaches offer unique opportunities to learn about continental deformation; however, each has limitations; the first approach ignores the deformation occurring in between major faults, while the second approach of treating deformation as continuous poses problems as it does not consider faults that represent the failure of the outermost brittle layer of the lithosphere.

Convective forces arising from mantle dynamics have also been invoked to explain surface deformation (Forte et al., 2010; Ghosh et al., 2013). However, trying to explain deformation with a completely fluid dynamical model poses a problem because of the presence of rigid plates. A combined model of lithosphere dynamics and mantle convection has been used to explain plate motions and lithospheric deformation by various studies (Bai et al., 1992; Bird, 1998; Bird et al., 2008; Finzel et al., 2015; Ghosh & Holt, 2012; Ghosh et al., 2008; 2013; 2013; Lithgow-Bertelloni & Guynn, 2004; Naliboff et al., 2012; Singh et al., 2017; Steinberger et al., 2001; Stotz et al., 2017; Wang et al., 2015, 2019).

In this paper, we use a numerical model that can explain the deformation of the Indian plate as well as the Indo-Eurasia collision zone. We investigate the relative roles of mantle and lithospheric forces that result in the observed deformation pattern of the region. We evaluate several density models and two viscosity structures to predict deviatoric stresses and plate velocities. We perform a quantitative comparison of our solutions to a range of surface observations such as plate velocities defined by GPS observations (Kreemer et al., 2014), strain rates from Global Strain Rate Model (GSRM; Kreemer et al., 2014), and SH_{max} (most compressive principal stress axes) directions and style from World Stress Map (WSM; Heidbach et al., 2016).

2. Method

The sources of stress within the lithosphere can be divided into two categories: (i) stresses due to GPE variations and (ii) stresses associated with basal tractions arising from density driven mantle convection. Differences in GPE result from lateral density variations within the lithosphere due to varying crustal thickness and topography. The spatial variation of GPE leads to horizontal flow from high to low GPE areas that produce deviatoric stresses within the lithosphere (Artyushkov, 1973; Coblenz et al., 1994; Fleitout & Froidevaux, 1982, 1983; Frank, 1972; Richardson, 1992). Density-driven mantle convection produces shear

tractions that act at the base of the lithosphere generating a second stress field, which, when combined with the GPE related stresses, constitutes the total lithospheric stress field.

2.1. The Lithosphere Model

The finite element (FE) model we use in this study solves the force balance equation:

$$\frac{\partial \sigma_{ij}}{\partial x_j} + \rho g_i = 0 \quad (1)$$

where σ_{ij} is the ij th component of the total stress tensor, x_j is the j^{th} coordinate axis, ρ is the density, and g_i is the acceleration due to gravity. Equation (1) uses summation notation, where i denotes the values of x , y , and z , and the index j represents the repeated summation over x , y , and z . We solve these equations in spherical coordinates as in Ghosh et al. (2013).

We expand equation (1) in z direction and integrate it from surface to a uniform reference level L . We then use the thin sheet approximation, which states that

$$\frac{\partial}{\partial x} \int_{-h}^L \sigma_{xz} dz + \frac{\partial}{\partial y} \int_{-h}^L \sigma_{yz} dz \ll - \int_{-h}^L \rho g_z dz \quad (2)$$

and obtain the vertical stress (σ_{zz}) as

$$\sigma_{zz} = - \int_{-h}^z \rho(z') g dz' \quad (3)$$

We substitute the total stress, σ_{ij} , in equation (1) by deviatoric stresses, τ_{ij} , using the relationship, $\tau_{ij} = \sigma_{ij} - \frac{1}{3}\sigma_{kk}\delta_{ij}$, where δ_{ij} is the Kronecker delta, and $\frac{1}{3}\sigma_{kk}$ is the mean stress. We integrate equation (1) up to a common reference level (L), which is assumed to be the base of the lithosphere (~ 100 km). The resultant full horizontal force balance equations can be written as

$$\frac{\partial \bar{\tau}_{xx}}{\partial x} - \frac{\partial \bar{\tau}_{zz}}{\partial x} + \frac{\partial \bar{\tau}_{xy}}{\partial y} = - \frac{\partial \bar{\sigma}_{zz}}{\partial x} + \tau_{xz}(L) \quad (4)$$

$$\frac{\partial \bar{\tau}_{yx}}{\partial x} + \frac{\partial \bar{\tau}_{yy}}{\partial y} - \frac{\partial \bar{\tau}_{zz}}{\partial y} = - \frac{\partial \bar{\sigma}_{zz}}{\partial y} + \tau_{yz}(L) \quad (5)$$

where the over bars represent depth integration. The first terms on the right-hand side of equations (4) and (5) represent horizontal gradients in GPE per unit area, whereas $\tau_{xz}(L)$ and $\tau_{yz}(L)$ represent the tractions at the base of the thin sheet (lithosphere) at depth L , arising from density driven mantle convection (Ghosh et al., 2009).

In our study, we take the reference level to be 100 km below sea level. The contribution from both the forces, GPE and mantle tractions, when added, gives the total stress field. We use a FE technique on a global grid of $1^\circ \times 1^\circ$ based on the methodology of Flesch et al. (2001), to predict deviatoric stresses, so that we obtain a global minimum for the second invariant of deviatoric stress, while also including lateral viscosity variations in the lithosphere. In order to incorporate lateral strength variations, we introduce weak zones by assigning variable viscosities along plate boundaries, which are inversely proportional to strain rates obtained from Kreemer et al., 2014 (2014; see Ghosh et al., 2009). In addition, we also introduce high-viscosity cratons (10 times stronger than intraplate regions) from 3SMAC (Nataf & Ricard, 1996). We also assign temperature dependent viscosity to oceanic lithosphere in such a way that older (or colder) lithosphere is more viscous than younger (or warmer) one (Figure 2a).

We compute the vertically integrated vertical stress, $\bar{\sigma}_{zz}$ (the first term on the right-hand side of equations (4) and (5)), integrated from the top of variable topography up to a common reference depth (England & Molnar, 1997; Flesch et al., 2001; Ghosh et al., 2006, 2009), which is given by negative of GPE per unit area:

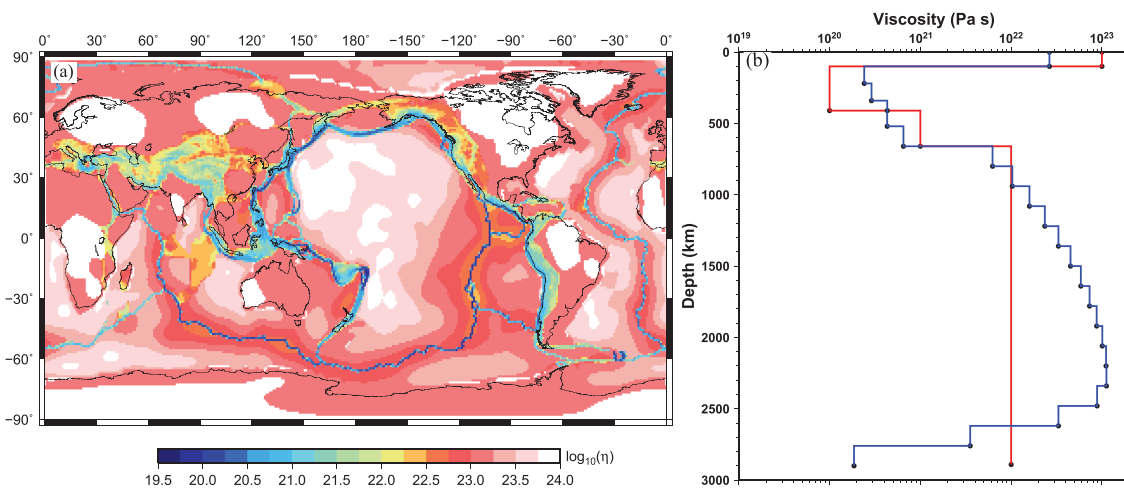


Figure 2. (a) Actual “best fit” viscosity values in pascal-second that result from the fitting of kinematic plate motions from Kreemer et al. (2014), and (b) radial viscosity structures, GHW13 (Ghosh et al., 2013; red) and SH08 (Steinberger & Holme, 2008; blue), used in the mantle convection models to calculate basal tractions.

$$\bar{\sigma}_{zz} = - \int_{-h}^L \left[\int_{-h}^z \rho(z') g dz' \right] dz = - \int_{-h}^L (L-z) \rho(z) g dz \quad (6)$$

Here, $\rho(z)$ is the density, L is the depth to the base of the thin sheet, h is the topographic elevation, z and z' are variables of integration, and g is the acceleration due to gravity. For a common reference level, we assume a depth of 100 km below sea level, but this depth can be varied. Integrating up to different depths will change the total GPE, but not the GPE differences and hence the associated deviatoric stresses will remain largely unaffected (Ghosh et al., 2009; Hirschberg et al., 2018; Jay et al., 2018; Klein et al., 2009). We calculate GPE using CRUST1.0 model (Laske et al., 2013) that gives the thickness and densities of various crustal layers on a $1^\circ \times 1^\circ$ global grid. A part of the present-day topography contains dynamic topography, which arises due to radial tractions resulting from density-driven mantle flow. Hence, GPE also contains contribution from radial tractions, unless topography and/or density is adjusted to achieve compensation at a given depth (see Ghosh et al., 2013).

The lithospheric FE model also predicts the directions of relative plate motions and strain rates. The strain rate magnitudes and plate velocities are controlled by absolute values of viscosity. These absolute viscosity values are computed by a postprocessing step where we place the predicted velocity field in a no-net-rotation (NNR) frame so that $\int (v \times r) dS = 0$, where v is the horizontal surface velocity at position r and S is the area over the Earth’s surface (see Ghosh et al., 2013, for details). We find the scaling factor for the viscosity field that will minimize the misfit between the dynamic (predicted) velocity field and the kinematic velocity field from Kreemer et al. (2014) in an NNR frame.

2.2. Mantle Convection Model

We use a semianalytical, spherical global mantle flow model, HC (Hager & O’Connell, 1981; Milner et al., 2009), where flow is driven by density anomalies derived from seismic tomography models to compute the basal tractions. To calculate mantle circulation using HC, we require three inputs: mantle density anomalies inferred from seismic tomography models, radial viscosity structure, and seismic velocity-density scaling ($d\ln\rho/d\ln v$). The density variations in our mantle flow model are derived by converting seismic velocities in tomography models to densities by using a velocity-density scaling. The seismic tomography models used as input in HC are S40RTS (Ritsema et al., 2011), SEMUCB-WM1 (French & Romanowicz, 2015), MITP_2016MAY (Burdick et al., 2017), SAW642AN (Mégnin & Romanowicz, 2000a; Figure 3). We also use a regional P wave tomography model by Singh et al. (2014) merged with SAW642AN in the Indian plate region, which we refer to as SINGH_SAW model throughout the paper (Figure 3d). We rescale the velocity anomalies of both the models to obtain comparable velocity amplitudes. We apply a smoothing filter at the boundaries of the merged models in order to avoid any sudden jumps. We repeat the same exercise with

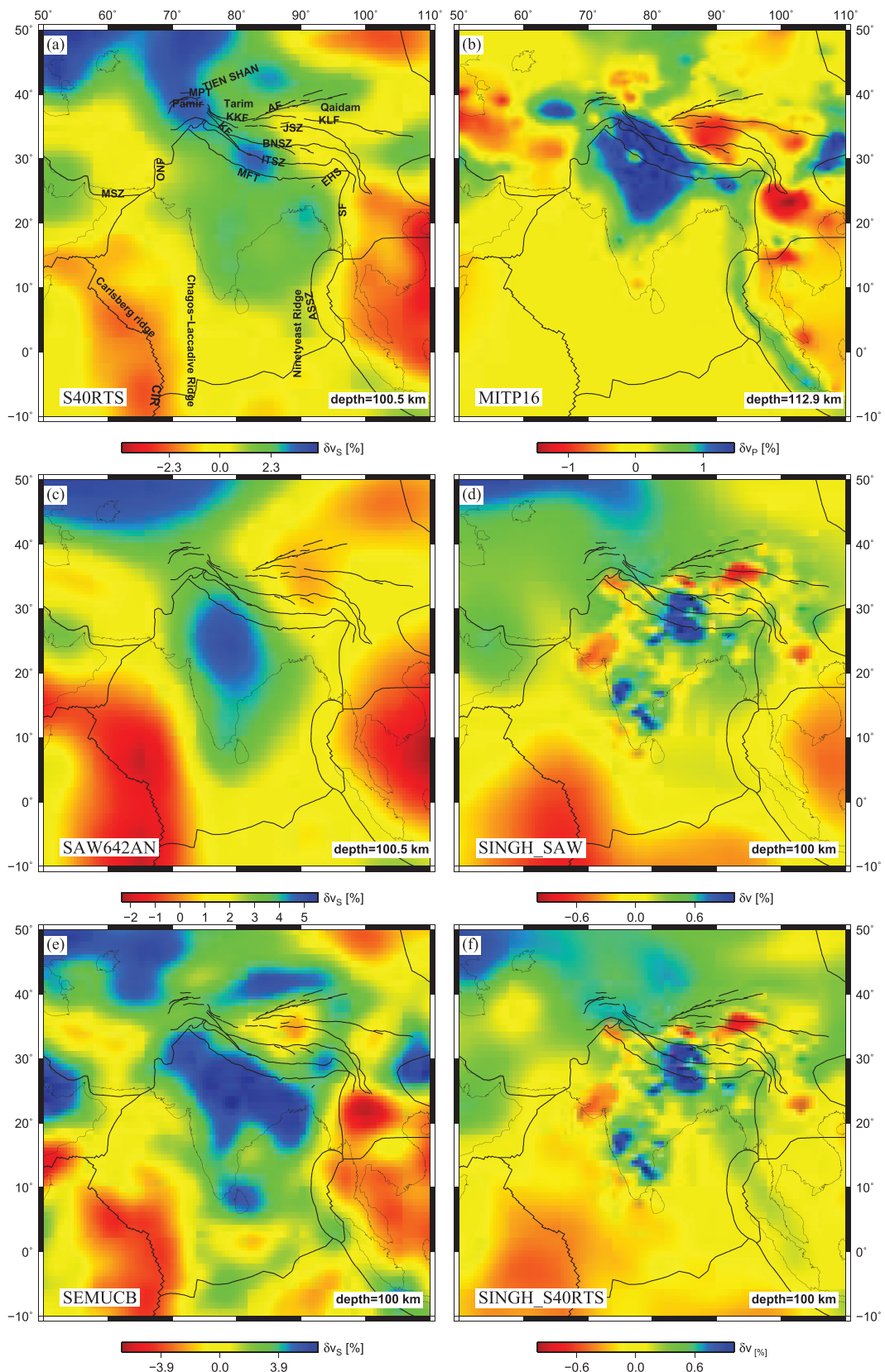


Figure 3. Tomography images at a depth of ~ 100 km from (a) S40RTS (Ritsema et al., 2011), (b) MITP_2016MAY (Burdick et al., 2017), (c) SAW642AN (Mégnin & Romanowicz, 2000b), (d) SINGH_SAW, (e) SEMUCB-WM1 (French & Romanowicz, 2015), and (f) SINGH_S40RTS seismic models for India and Eurasia region.

S40RTS model, which yields the combined model, SINGH_S40RTS (Figure 3f). SAW642AN and S40RTS were evaluated as the best tomography models that gave an optimum fit to the global geoid, plate motion, and strain rates in an earlier study by Wang et al. (2015).

Radial viscosity variations are an important aspect of mantle circulation models. Here, we use two radial viscosity structures: GHW13, which is the best model of Ghosh et al. (2013), and SH08 (Steinberger & Holme, 2008; Figure 2b). GHW13 is a four-layer model that contains a highly viscous lithosphere ($\sim 10^{23}$ Pa s) with a low-viscosity asthenosphere ($\sim 10^{20}$ Pa s) and a high-viscosity lower mantle (Figure 2b). SH08 has a slightly weaker lithosphere than GHW13, and there is a gradual increase in viscosity with depth, with the highest viscosity (10^{23} Pa s) in the lower mantle occurring at $\sim 2,000$ – $2,300$ km. Also, there is a large drop in viscosity in the lowermost mantle around the D'' layer (Figure 2b). The HC code does not incorporate lateral viscosity variations. However, they are incorporated in our FE model (Figure 2a). The boundary conditions we use are free slip at the surface and at the core-mantle boundary. The tangential stresses obtained from HC at the base of the lithosphere (~ 100 km) are used as effective body force equivalents that are applied as boundary condition at the base of the lithosphere in our FE model (equations (4) and (5)). The solutions to these equations yield the total deviatoric stress field.

3. Surface Observations Used as Constraints

We use the strain rates from GSRM v.2.1 (Kreemer et al., 2014) and SH_{max} (most compressive horizontal principal axes) stresses from the WSM (Heidbach et al., 2016) as constraints in order to evaluate predicted deviatoric stresses in our study area. We also use plate velocities from Kreemer et al. (2014) as an additional constraint. GSRM v.2.1 is an improved and higher resolution version of the older GSRM, based on GPS measurements (Figures 4a and 4b). The original strain rates are on a $0.1^\circ \times 0.1^\circ$ grid, which we interpolate on our $1^\circ \times 1^\circ$ grid with a smoothing function. We compare our predicted deviatoric stresses with the GSRM strain rates using the following equation (Flesch et al., 2007; Ghosh et al., 2008, 2013)

$$-1 \leq \sum_{\text{areas}} (\epsilon \cdot \tau) \Delta S / \left(\sqrt{\sum_{\text{areas}} (E^2) \Delta S^*} \sqrt{\sum_{\text{areas}} (T^2) \Delta S} \right) \leq 1 \quad (7)$$

where

$$E = \sqrt{\dot{\epsilon}_{\phi\phi}^2 + \dot{\epsilon}_{\theta\theta}^2 + \dot{\epsilon}_{rr}^2 + \dot{\epsilon}_{\phi\theta}^2 + \dot{\epsilon}_{\theta r}^2} = \sqrt{2\dot{\epsilon}_{\phi\phi}^2 + 2\dot{\epsilon}_{\phi\theta}\dot{\epsilon}_{\theta\theta} + 2\dot{\epsilon}_{\theta\theta}^2 + 2\dot{\epsilon}_{\theta r}^2},$$

$$T = \sqrt{\tau_{\phi\phi}^2 + \tau_{\theta\theta}^2 + \tau_{rr}^2 + \tau_{\phi\theta}^2 + \tau_{\theta r}^2} = \sqrt{2\tau_{\phi\phi}^2 + 2\tau_{\phi\theta}\tau_{\theta\theta} + 2\tau_{\theta\theta}^2 + 2\tau_{\theta r}^2}, \text{ and}$$

$$\epsilon \cdot \tau = 2\dot{\epsilon}_{\phi\phi}\tau_{\phi\phi} + \dot{\epsilon}_{\phi\theta}\tau_{\theta\theta} + \dot{\epsilon}_{\theta\theta}\tau_{\phi\phi} + 2\dot{\epsilon}_{\theta\theta}\tau_{\theta\theta} + 2\dot{\epsilon}_{\theta r}\tau_{\theta r}$$

Here E and T are second invariants of strain rate and stress tensors, $\dot{\epsilon}_{ij}$ are the strain rates from GSRM, ΔS is the area, and τ_{ij} are the predicted deviatoric stresses. Normalization is done in order to ensure that the correlation coefficient depends on the inferred style of faulting and direction of principal axes (Figure 4b) and not on the magnitudes of stress and strain. A correlation coefficient of 1 indicates a perfect fit between the principal axes direction as well as the expected style of faulting associated with the strain rate tensors and predicted deviatoric stresses. On the other hand, the minimum coefficient of -1 indicates anticorrelation, for example, strain rate tensor predicting a thrust regime, whereas modeled deviatoric stresses predicting an extensional regime (normal faulting). A correlation coefficient of -1 can also arise when both strain rates and stresses show similar style of faulting, but with orientations at right angles to each other. Strain rates and deviatoric stresses will be uncorrelated (correlation coefficient is zero), when, for example, in case of thrust or normal faulting areas, deviatoric stresses predicting strike-slip faulting. Alternatively, zero correlation can also occur when predicted principal stress axes differ from those in GSRM by 45° .

While the strain rates can constrain the stress models at the plate boundary zones and areas of diffuse continental deformation, they do not yield any information on the deformation of intraplate areas. Hence, we use the WSM data (Heidbach et al., 2016) as an additional constraint. WSM contains information on

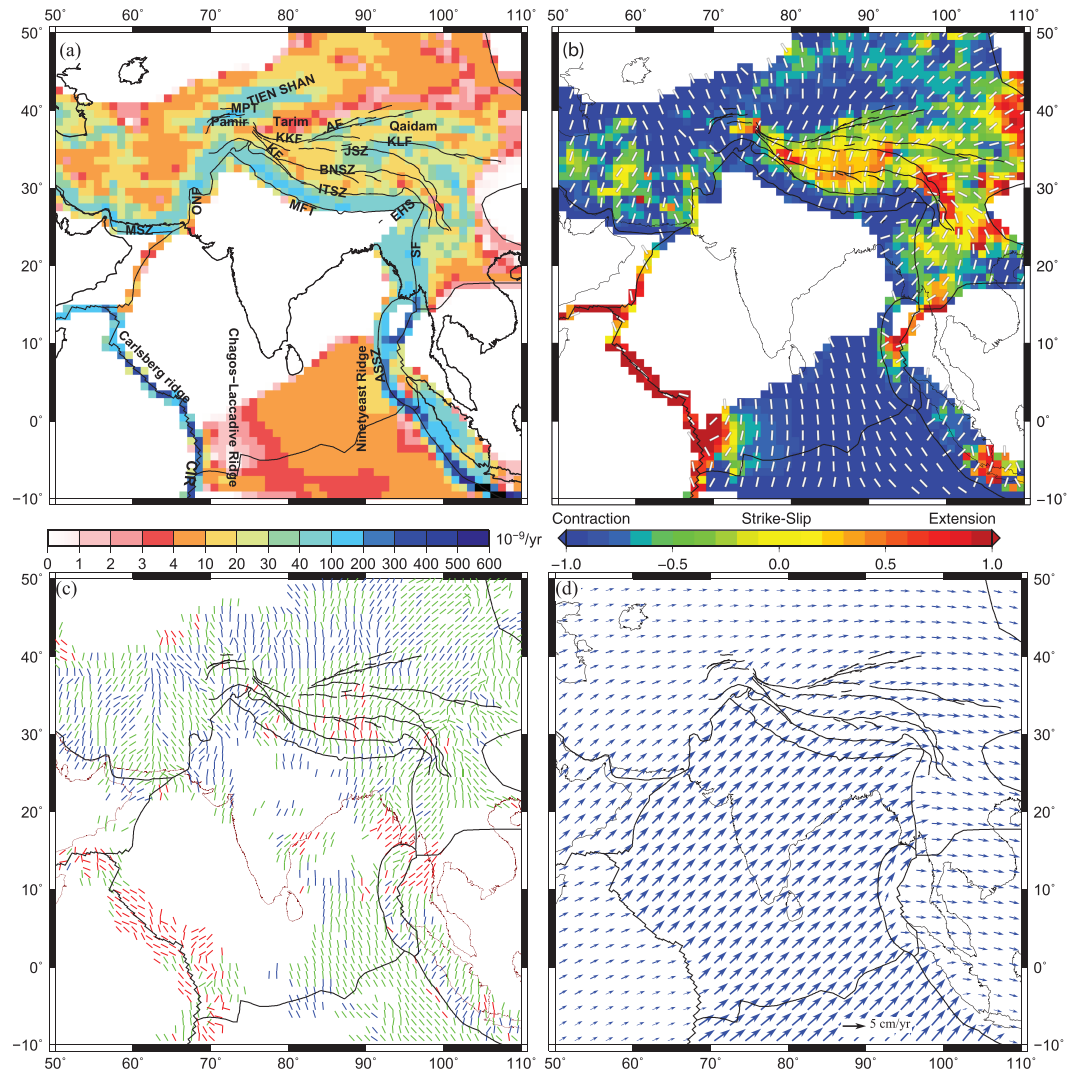


Figure 4. (a) Second invariant of strain rate tensors obtained from Kreemer et al. (2014) plotted on $1^\circ \times 1^\circ$ grid; (b) the principal axes directions calculated using strain rates (Kreemer et al., 2014), plotted on a measure of the style of the strain rate tensor. The style measure is defined by $(\dot{e}_1 + \dot{e}_2)/\max(|\dot{e}_1| |\dot{e}_2|)$, where \dot{e}_1 and \dot{e}_2 are the largest and smallest eigenvalues (Kreemer et al., 2014). As the value approaches to -1 , the regime transitions to contraction, while $+1$ indicates extension. (c) Most compressive horizontal principal axes (SH_{\max}) from World Stress Map (Heidbach et al., 2016), interpolated within $1^\circ \times 1^\circ$ areas. Red indicates normal fault regime, blue indicates thrust regime, whereas green denotes strike-slip regime. (d) Observed velocities in a no-net-rotation frame of reference from Kreemer et al. (2014). MFT = Main Frontal Thrust; MSZ = Makran Subduction Zone; MPT = Main Pamir Thrust; KKF = Karakax Fault; AF = Altn Tagh fault; KF = Karakorum Fault; KLF = Kunlun Fault; JSZ = Jinshajiang Suture Zone; BNSZ = Bangong-Nujiang Suture Zone; ONF = Ornach-Nal Fault; EHS = Eastern Himalayan Syntaxis; SF = Sagaing Fault; ASSZ = Andaman Sumatra subduction zone; CIR = Central Indian Ridge.

present-day lithospheric stress field and consists of the most compressive principal stress directions from earthquake focal mechanisms, borehole breakout data, and Quaternary fault slip data. We interpolate the WSM SH_{\max} data on our $1^\circ \times 1^\circ$ grid (Figure 4c) and compute the angular deviation (θ) between the observed and the predicted SH_{\max} directions. The angular misfit ranges between 0° (perfect fit) to 90° . Additionally, we compute a total misfit (ϵ_p ; Ghosh et al., 2013), given by $\sin\theta(1+R)$, where R is the regime misfit. R is calculated by assigning values between 1 and 3 to the SH_{\max} stresses based on whether they are tensional, strike slip, or compressional. Hence, the difference in regime misfit ranges from 0 to 2. The total misfit (ϵ_p) is a joint evaluation of both the angular and regime misfit and falls between 0 and 3. Finally, we also use the plate velocities from Kreemer et al. (2014) in a NNR frame, based on GPS

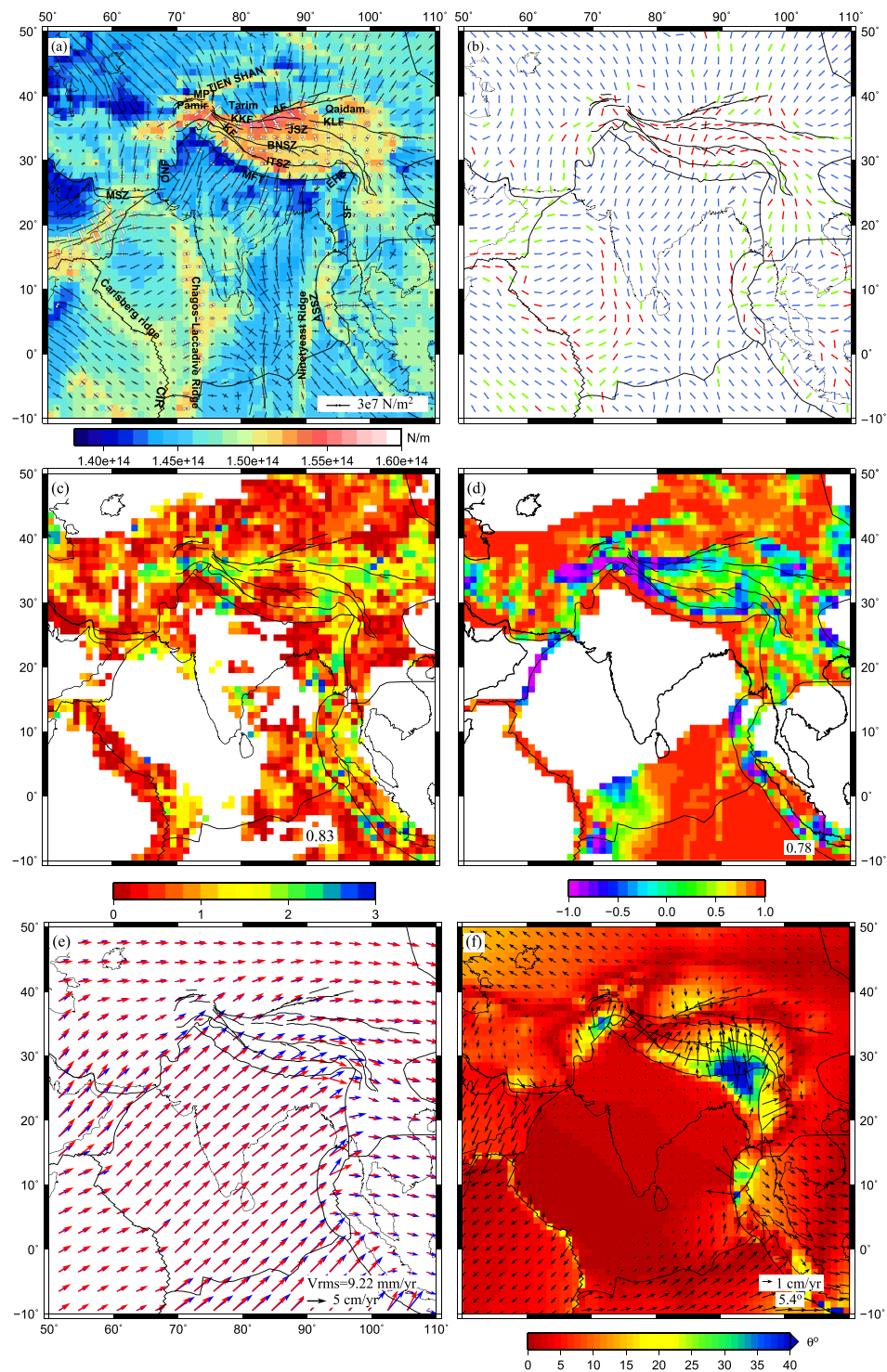


Figure 5. Parameters predicted from GPE variations and their comparisons with observables. (a) Deviatoric stresses plotted on top of GPE variations. The compressional stresses are denoted by solid black arrows, while white arrows show tensional stresses, (b) predicted SH_{\max} , red denotes tensional regime, blue is for thrust, and green for strike-slip regime. (c) Total misfit between predicted and observed SH_{\max} from World Stress Map. (d) Correlation between predicted stress tensors and Global Strain Rate Model strain rate tensors using equation (7), with average regional correlation coefficient given in bottom right, (e) predicted (red) and observed plate velocities (blue) from Kreemer et al. (2014), and (f) angular misfit between observed (Kreemer et al., 2014) and predicted plate velocities; the arrows show vector difference between them. The average angular deviation (θ) is given in the bottom right of the figure. GPE = gravitational potential energy. MFT = Main Frontal Thrust; MSZ = Makran Subduction Zone; MPT = Main Pamir Thrust; KKF = Karakax Fault; AF = Altn Tagh fault; KF = Karakorum Fault; KLF = Kunlun Fault; JSZ = Jinshajiang Suture Zone; BNSZ = Bangong-Nujiang Suture Zone; ONF = Ornach-Nal Fault; EHS = Eastern Himalayan Syntaxis; SF = Sagaing Fault; ASSZ = Andaman Sumatra subduction zone; CIR = Central Indian Ridge.

Table 1
Summary of Results for Various Models

Models		SH _{max}	Plate velocities			Total error
			Total misfit (ϵ_p)	Strain rate corr.	RMS error (mm/year)	
Combined model (GPE + mantle tractions)	GPE Only	0.83	0.78	9.22	5.4°	2.01
		S40RTS	0.61	0.89	6.59	6.4°
		SAW642AN	0.65	0.82	8.43	6.2°
		GHW13	0.65	0.86	7.44	7.0°
		SEMUCB	0.71	0.83	7.09	5.7°
	SH08	MITP16	0.63	0.84	8.00	7.0°
		SINGH_SAW	0.60	0.88	6.22	4.6°
		SINGH_S40RTS	0.67	0.87	7.66	7.0°
		S40RTS	0.70	0.82	8.64	7.2°
		SAW642AN	0.69	0.85	8.92	8.3°
	viscosity	SEMUCB	0.78	0.82	7.60	5.4°
		MITP16	0.72	0.80	8.54	8.6°
		SINGH_SAW	0.72	0.85	7.91	5.3°
		SINGH_S40RTS	0.77			1.77

Note. GPE = gravitational potential energy; RMS = root-mean-square.

observations, to constrain our models. We calculate the angular misfit between the predicted plate velocities and the observed velocities (Figure 4d) that yields values between 0° and 180°. We also calculate an root-mean-square (RMS) misfit (Ghosh & Holt, 2012; Ghosh et al., 2013) over the region of interest between the predicted and observed plate velocities.

4. Results

4.1. Predicting Parameters Using GPE Contribution

The deviatoric stresses resulting from GPE differences (Figure 5a), which are calculated from the CRUST1.0 model, show extension in regions of high GPE (elevated regions) and compression in areas of low GPE. The largest tensional deviatoric stress is observed in the Tibetan plateau. Southwestern Tibet shows E-W tension, which becomes more N-S directed toward the east. Qaidam basin shows dominantly NW-SE tension whereas the Tarim Basin shows NW-SE compression. Pure tension is observed in the Pamir region as also seen by Jay et al. (2017) and Jay et al. (2018). In the east, the Sagaing fault shows E-W compression whereas dominantly N-S compression is seen in the Bengal fan. Within India itself, we observe predominant NNW-ESE compression within peninsular India and NE-SW compressional stresses closer to the collisional boundary in the north. The oceanic part of the Indian plate is dominantly compressional except for the Carlsberg and Chagos-Laccadive ridges which show relatively high GPE and tensional stresses. Figure 5b shows the regime of faulting and the orientation of the SH_{max} axes from the predicted deviatoric stresses, clearly indicating dominant tension in Tibet and a rotation of the SH_{max} axes near the EHS. It also shows the majority of the Indian plate to be in compression with the exception of the Chagos-Laccadive ridge that displays E-W tension (Figure 5b).

When we consider the total misfit that takes into account both the angular difference and the regime misfit between the predicted SH_{max} and those obtained from WSM, we obtain a value of 0.83 (Figure 5c). The total misfit is quite low (<1) in most areas except for a few places such as the western and the eastern ends of the Tibetan plateau and the EHS. The correlation with strain rates from Kreemer et al. (2014) shows excellent fit along the Himalayas, central Tibet, the Carlsberg ridge, and the IAP deformation zone in the Indian Ocean, indicating that the deviatoric stresses predicted using GPE contributions are able to match the observed direction and style of faulting in these regions (Figure 5d). However, poor correlation is observed in most of the remaining part of Tibet, along the India-Arabia plate boundary zone, western part of IAP deformation zone and in the vicinity of the ASSZ, suggesting that GPE differences are not solely responsible for causing deformation in these regions. The average correlation coefficient for the region is 0.78.

The predicted velocities match closely with the observed velocities in most places with an average regional RMS error of less than 1 cm/year (Figure 5e) and an average angular misfit of 5.4° (Figure 5f). However, some misfit occurs within the Tibetan plateau where the predicted velocities from GPE are more easterly than what is actually observed. A large misfit of >30° also occurs near the EHS. The arrows in Figure 5f signify the vectors that need to be added to the predicted velocity vectors so that they match the observed velocities. For example, it is clearly seen that the predicted velocities near the EHS require a ~2–3 cm of northerly component in order to fit the kinematic plate velocities. Similarly, a northeasterly component of velocity needs to be added to the dynamic velocities in western Tibet so that they match the observed plate velocities. In some places (such as the IAP boundary region), although the angular misfit is low, there still occurs a mismatch in magnitudes of predicted dynamic and kinematic velocities. The overall results obtained using GPE contributions only are summarised in Table 1.

4.2. Predicting Parameters Using a Combined Model of GPE and Mantle Buoyancies

Although GPE derived stresses and velocities could match the observables fairly well, we wanted to test whether the existing misfits could be explained by adding the contribution from basal tractions arising from mantle flow. The deviatoric stresses from these basal tractions calculated using the FE lithosphere model are then added to those from GPE variations in order to yield a combined deviatoric stress field (equations (4) and (5)).

The introduction of mantle-derived deviatoric stresses increase the total deviatoric stress magnitudes considerably almost everywhere (Figure 6) with the GHW13 viscosity model yielding higher stresses compared to SH08. Within the Tibetan plateau, the stresses associated with mantle tractions introduce N-S compression, which cancels out the N-S components of tensional stresses in areas with high GPE in Tibet. Thus, the stresses change from predominantly tensional to more strike-slip in nature for all models, but especially for the S wave models, which is what we observe in Tibet. Within peninsular India as well, the NNW-ESE oriented compressional stresses from GPE variations give way to strike-slip types of stresses except for MITP2016 and SINGH_S40RTS+SH08. For all density models, the highest stress magnitudes occur within the Indian mainland, especially close to the eastern and western corners of the collisional front in the north (Figure 6). Large stresses are also seen within the deforming region of the Indian Ocean. The southeastern Indian Ocean shows strong NNW-SSE compression similar to what is observed in the WSM. The western part of the Indian Ocean, on the other hand, shows either strike-slip or tensional stresses. A strike-slip regime is observed east of the ASSZ, whereas the Carlsberg ridge shows ridge perpendicular tension. The two viscosity structures also yield slightly different deviatoric stresses for the same density model. The SH08 model introduces less compression in Tibet, so that northern Tibet still displays tensional stresses, especially for the P wave models (Figures 7g–7l). For SINGH_SAW model, the tensional stresses in the western Indian Ocean changes to more strike-slip with the SH08 viscosity structure. SINGH_S40RTS shows predominantly strike-slip stresses in the western Indian Ocean with the GHW13 viscosity structure (Figure 7k) that changes to compression with the SH08 viscosity structure (Figure 7l).

On comparing the predicted SH_{max} directions and style with those in the WSM, we find that the total misfit for all the models to be quite low (<1; Figure 8). The GHW13 viscosity structure yields lower misfit for all the density models compared to SH08, with the SINGH_S40RTS model showing the lowest misfit of 0.60 (Figure 8k). S40RTS also shows an excellent fit with an average total misfit of ~0.61 with GHW13 (Figure 8a). In Tibet and the Himalayas, the misfit is quite low except near the EHS. Compared to GPE derived stresses, the total fit improves for all the cases, with significantly reduced misfits obtained in the Tibetan Plateau and ASSZ.

The comparison between the predicted deviatoric stress tensors and the strain rate tensors shows a marked improvement of fit within Tibet for the combined models compared to the GPE only model, especially for S40RTS and SAW642AN, although eastern Tibet still shows some misfit (Figure 9). The fit is quite poor in the southwestern part of the Indian Ocean close to the Chagos-Laccadive ridge where the NW-SE extension of the GSRM strain rates along the Carlsberg ridge transform to N-S compression (Figure 4b). The fit along the ASSZ also improves for most models compared to GPE only case. However, most models fail to improve the fit along the India-Arabia plate boundary zone. S40RTS yields the highest correlation of 0.89 among all the models (Figure 9a). SINGH_S40RTS is a close second with a correlation coefficient of 0.88 (Figure 9k).

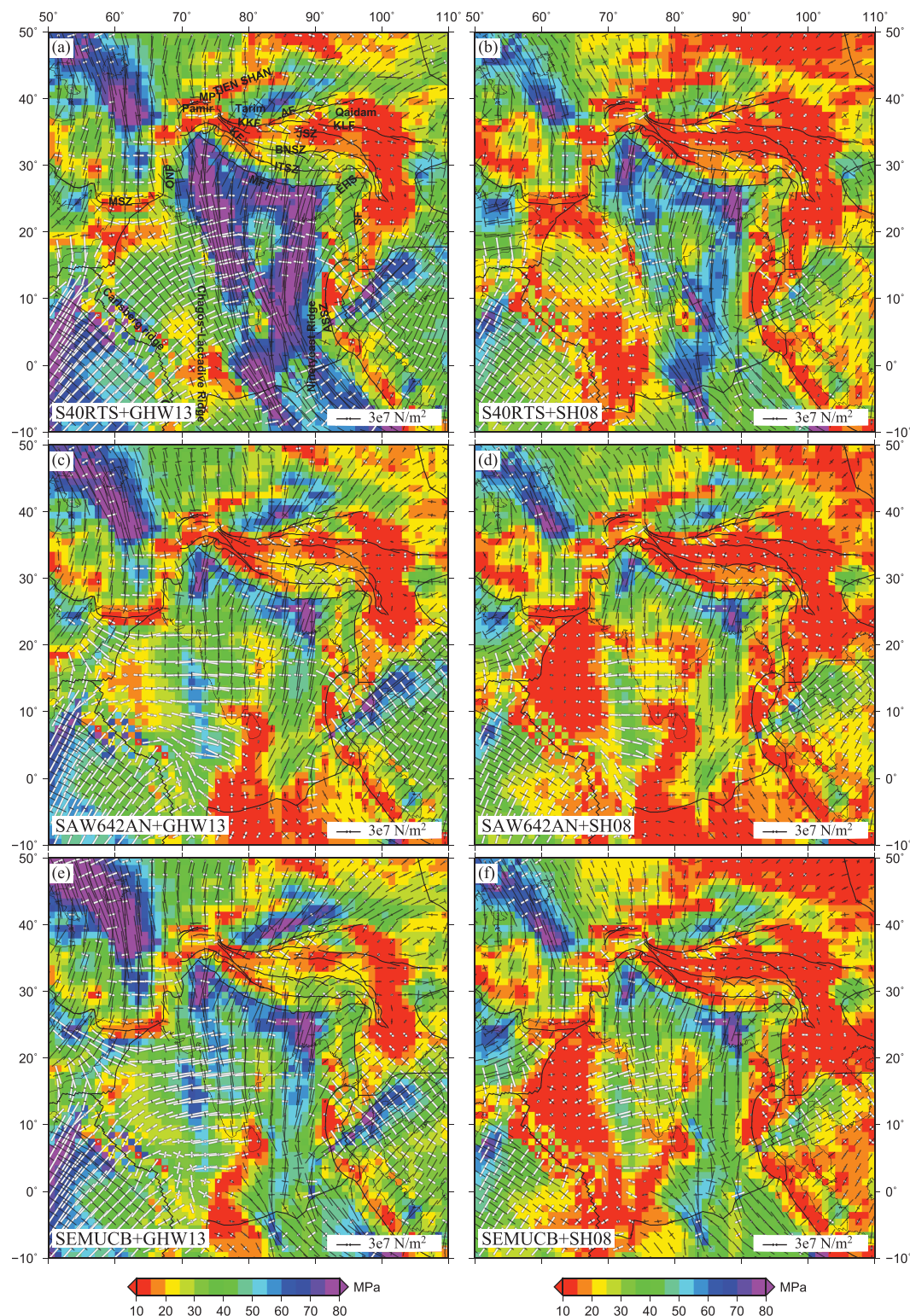


Figure 6. Deviatoric stresses predicted using combined effects of gravitational potential energy and mantle tractions derived from various tomography models for viscosity structures: GHW13 (a, c, e, g, i, and k) and SH08 (b, d, f, h, j, and l) plotted on second invariant of deviatoric stresses. The white arrows denote tensional stresses, and black arrows indicate compressional stresses. MFT = Main Frontal Thrust; MSZ = Makran Subduction Zone; MPT = Main Pamir Thrust; KFK = Karakax Fault; AF = Altyn Tagh fault; KF = Karakorum Fault; KLF = Kunlun Fault; JSZ = Jinshajiang Suture Zone; BNSZ = Bangong-Nujiang Suture Zone; ONF = Ornach-Nal Fault; EHS = Eastern Himalayan Syntaxis; SF = Sagaing Fault; ASSZ = Andaman Sumatra subduction zone; CIR = Central Indian Ridge.

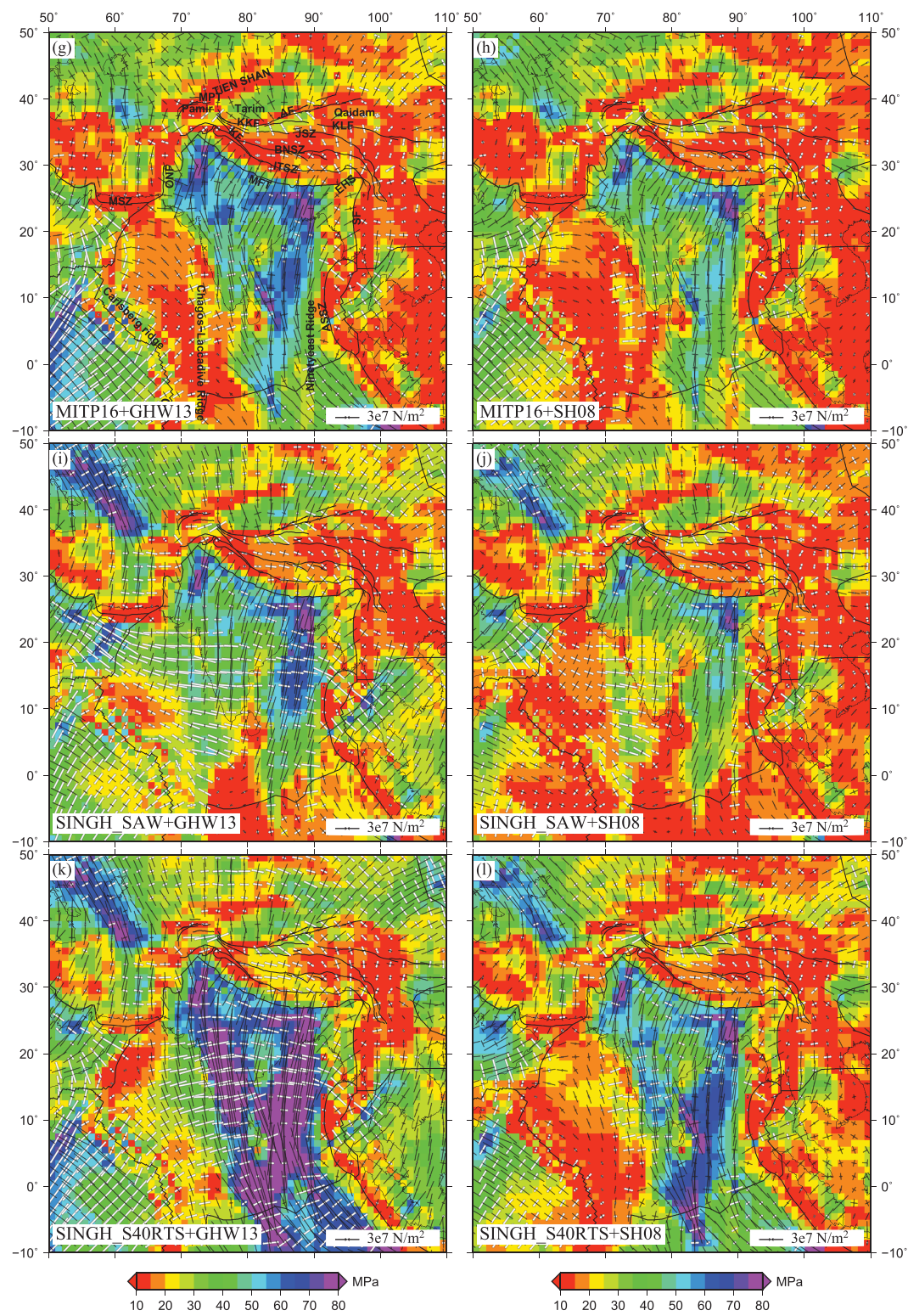


Figure 6. (continued)

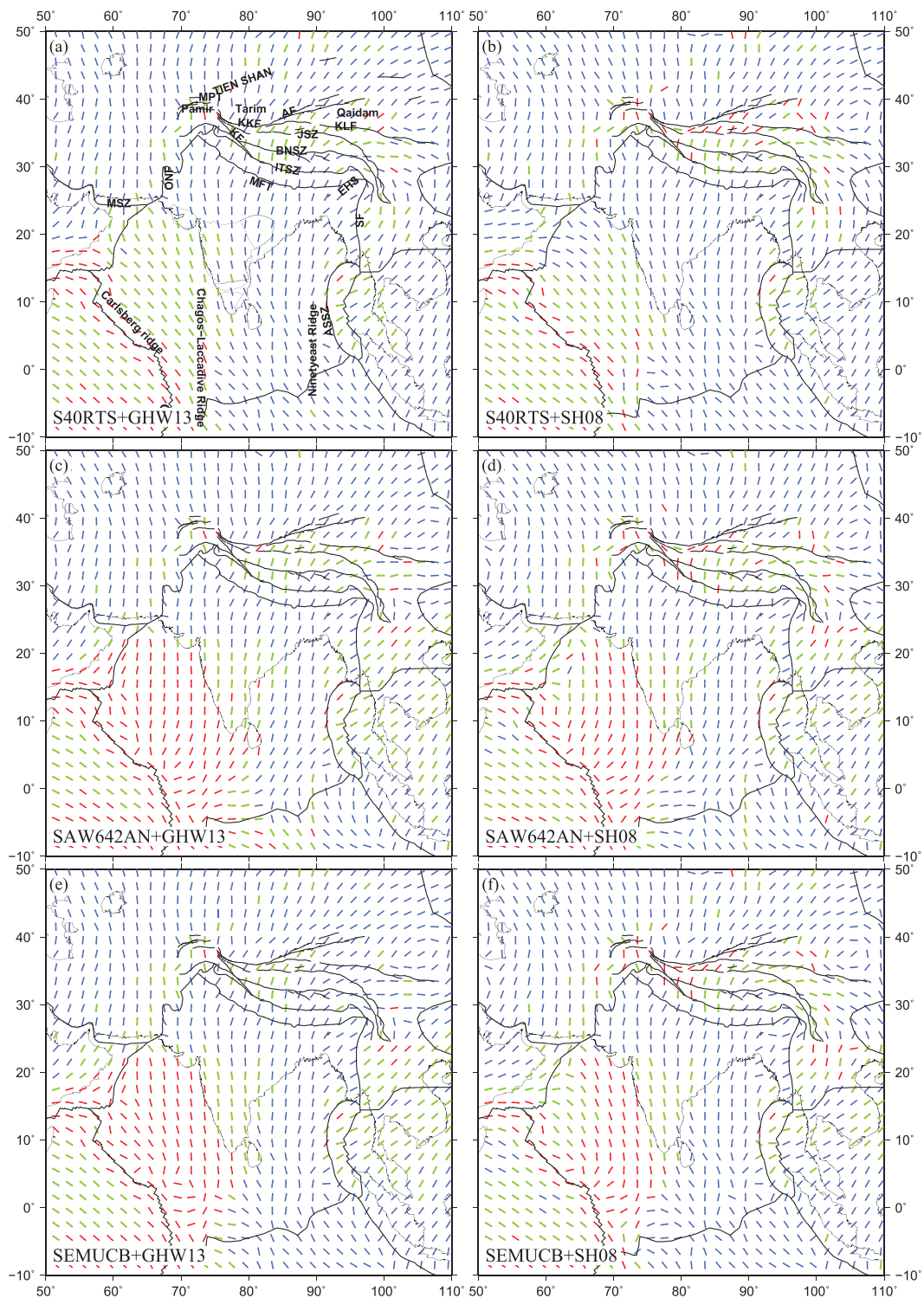


Figure 7. SH_{max} predicted using combined effects of gravitational potential energy and mantle tractions derived from various tomography models for viscosity structures: GHW13 (a, c, e, g, i, and k) and SH08 (b, d, f, h, j, and l). Red denotes tensional regime, blue is for thrust, and green is for strike-slip regime. MFT = Main Frontal Thrust; MSZ = Makran Subduction Zone; MPT = Main Pamir Thrust; KKF = Karakax Fault; AF = Altyn Tagh fault; KF = Karakorum Fault; KLF = Kunlun Fault; JSZ = Jinshajiang Suture Zone; BNSZ = Bangong-Nujiang Suture Zone; ONF = Ornach-Nal Fault; EHS = Eastern Himalayan Syntaxis; SF = Sagaing Fault; ASSZ = Andaman Sumatra subduction zone; CIR = Central Indian Ridge.

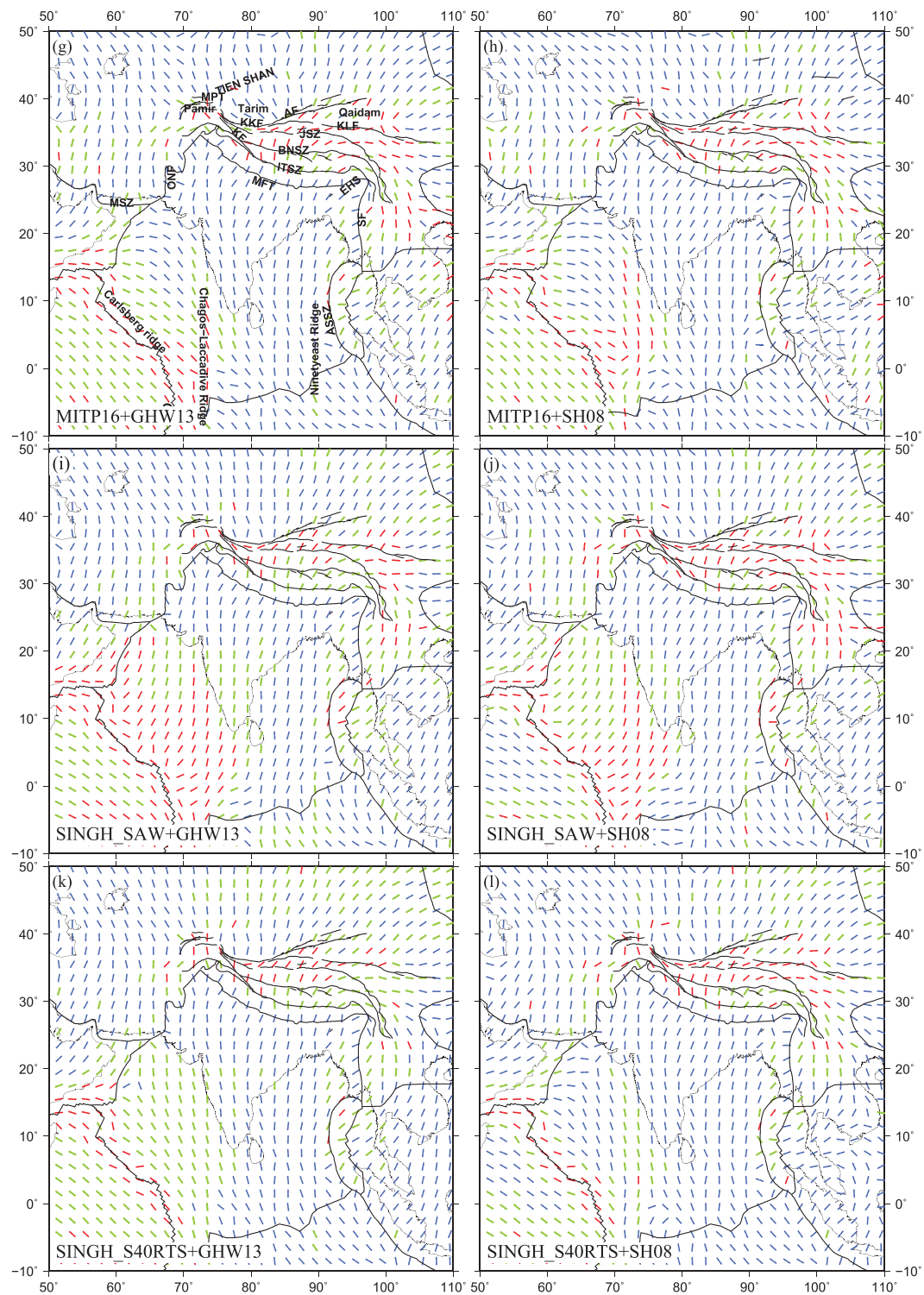


Figure 7. (continued)

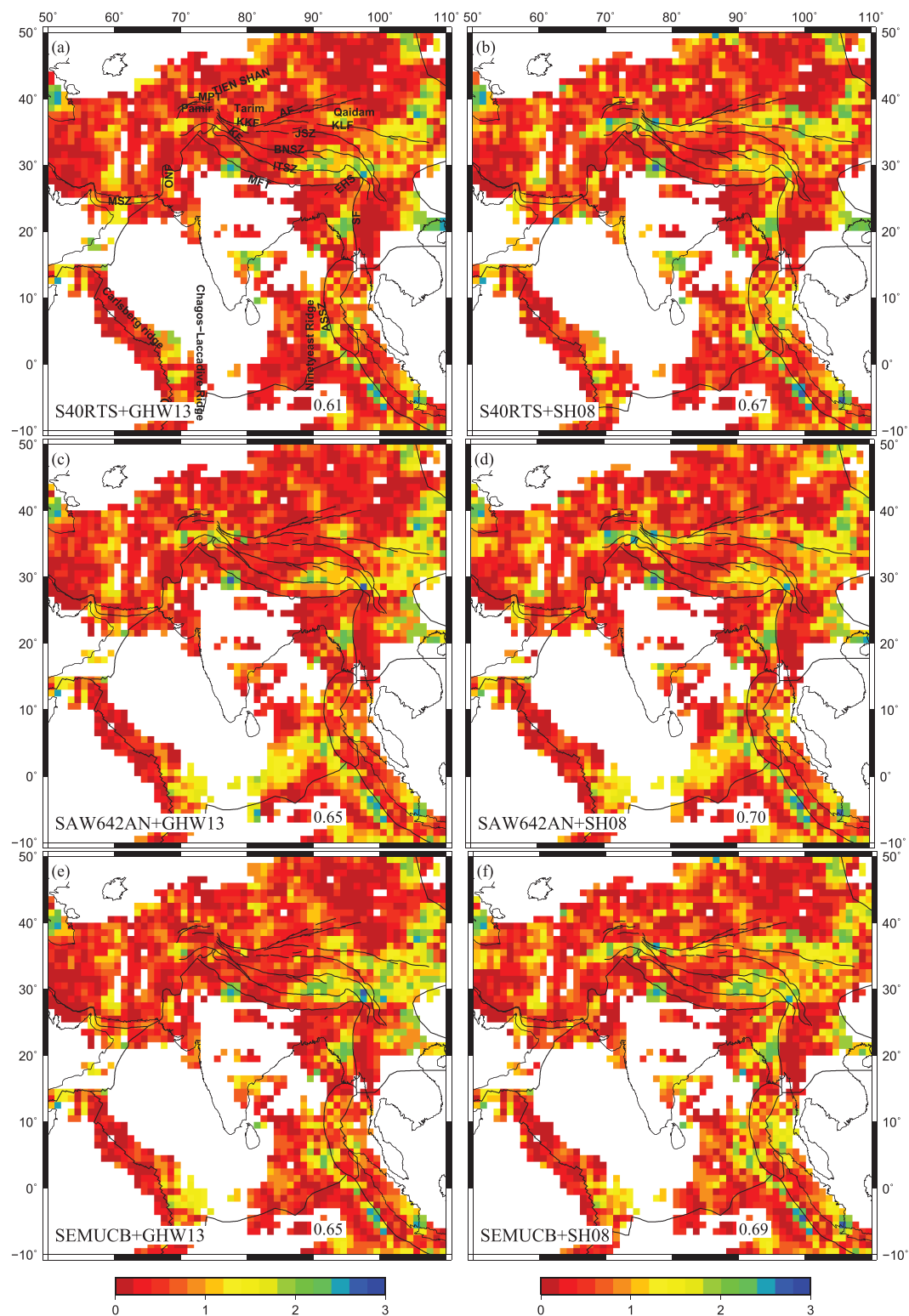


Figure 8. Total misfit between SH_{max} obtained from World Stress Map (Heidbach et al., 2016) and those predicted using combined model of gravitational potential energy and mantle tractions derived from various tomography models using viscosity structures: GHW13 (a, c, e, g, i, and k) and SH08 (b, d, f, h, j, and l). MFT = Main Frontal Thrust; MSZ = Makran Subduction Zone; MPT = Main Pamir Thrust; KKF = Karakax Fault; AF = Altyn Tagh fault; KF = Karakorum Fault; KLF = Kunlun Fault; JSZ = Jinshajiang Suture Zone; BNSZ = Bangong-Nujiang Suture Zone; ONF = Ornach-Nal Fault; EHS = Eastern Himalayan Syntaxis; SF = Sagaing Fault; ASSZ = Andaman Sumatra subduction zone; CIR = Central Indian Ridge.

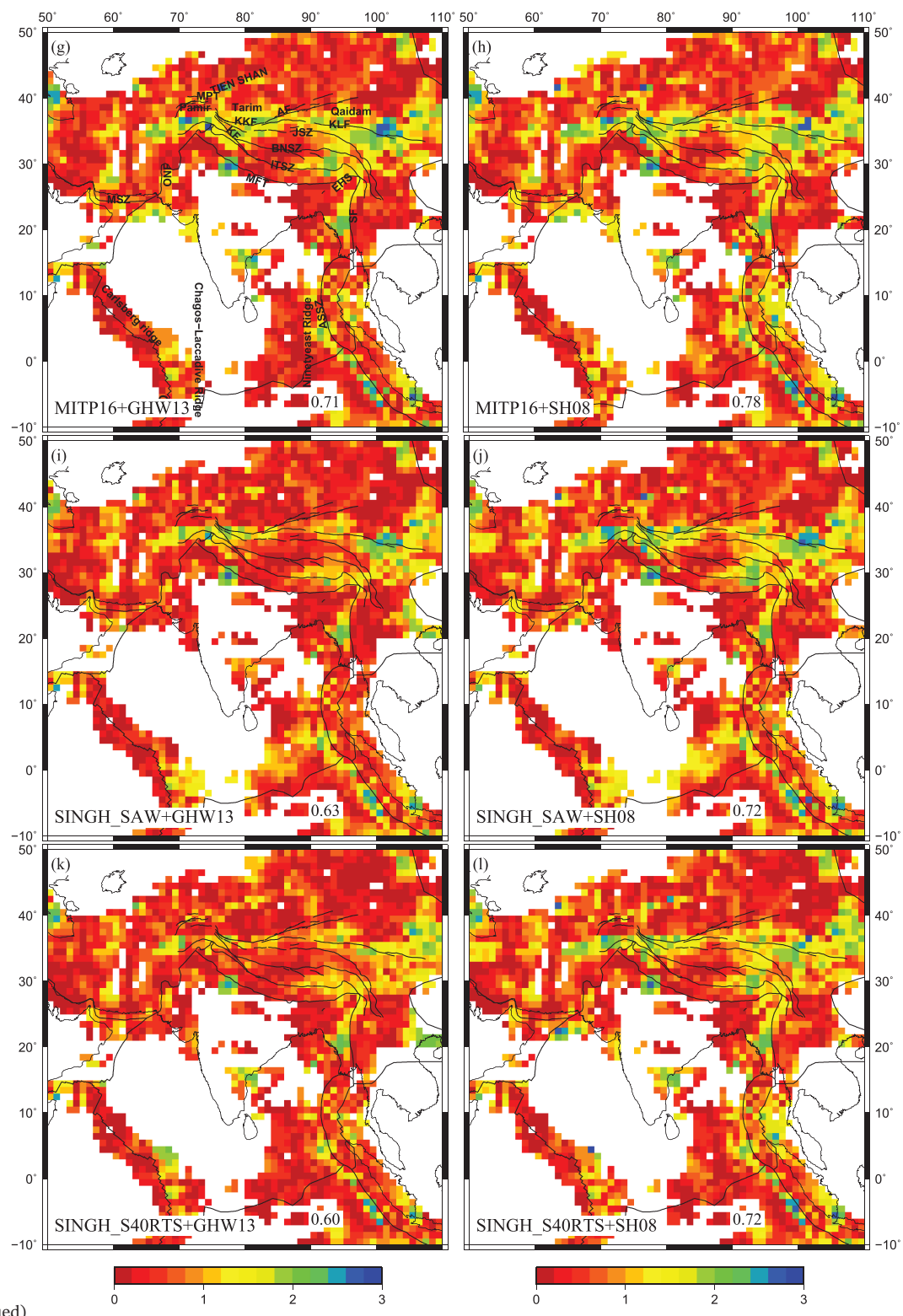


Figure 8. (continued)

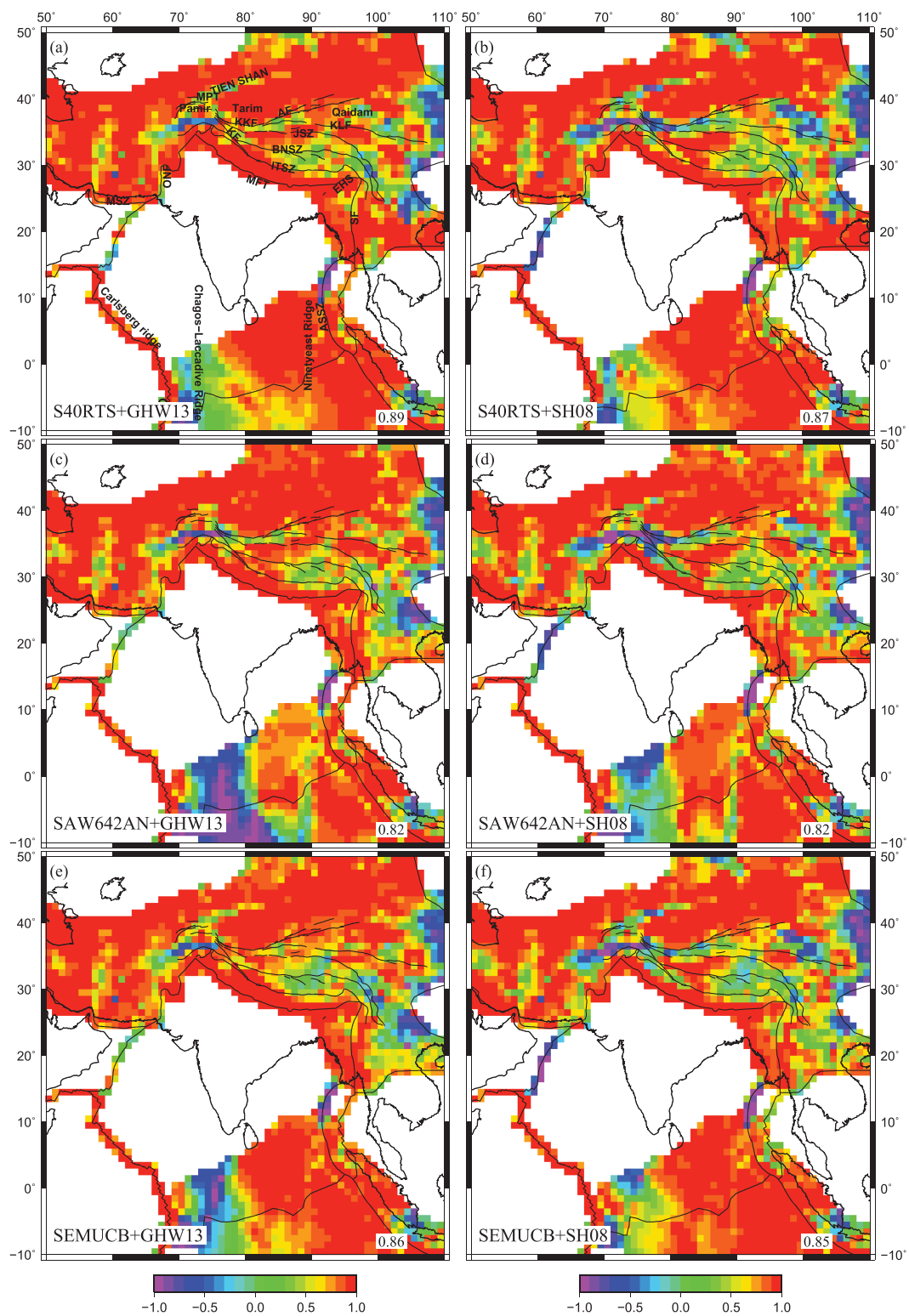


Figure 9. Correlation coefficients between strain rate tensors obtained from Kreemer et al. (2014) and deviatoric stresses predicted using combined model of gravitational potential energy and basal tractions derived from various tomography models for viscosity structures: GHW13 (a, c, e, g, i, and k) and SH08 (b, d, f, h, j, and l), with average regional correlation coefficients given on bottom right of each figure. MFT = Main Frontal Thrust; MSZ = Makran Subduction Zone; MPT = Main Pamir Thrust; KFK = Karakax Fault; AF = Altyn Tagh fault; KF = Karakorum Fault; KLF = Kunlun Fault; JSZ = Jinshajiang Suture Zone; BNSZ = Bangong-Nujiang Suture Zone; ONF = Ornach-Nal Fault; EHS = Eastern Himalayan Syntaxis; SF = Sagaing Fault; ASSZ = Andaman Sumatra subduction zone; CIR = Central Indian Ridge.

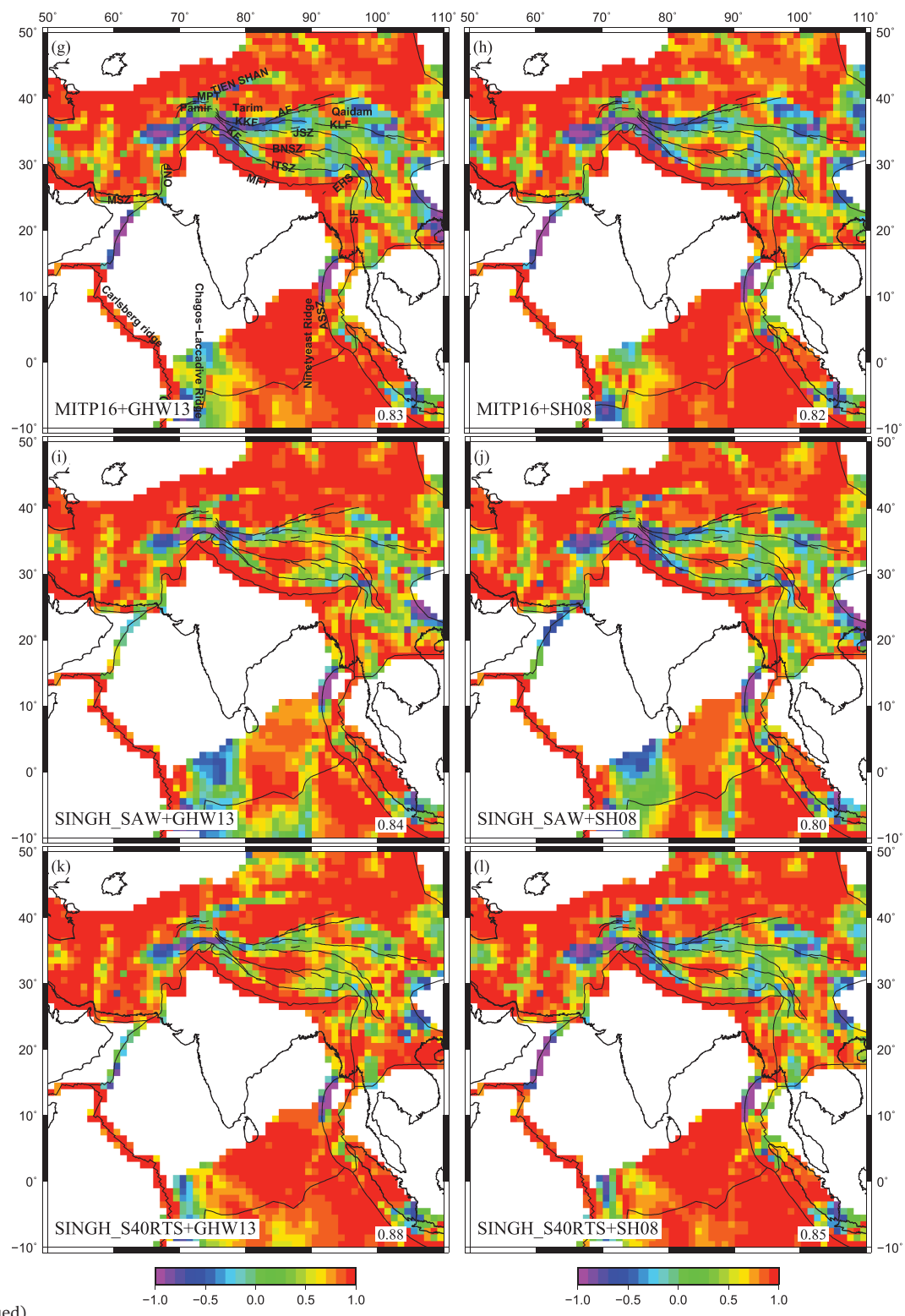


Figure 9. (continued)

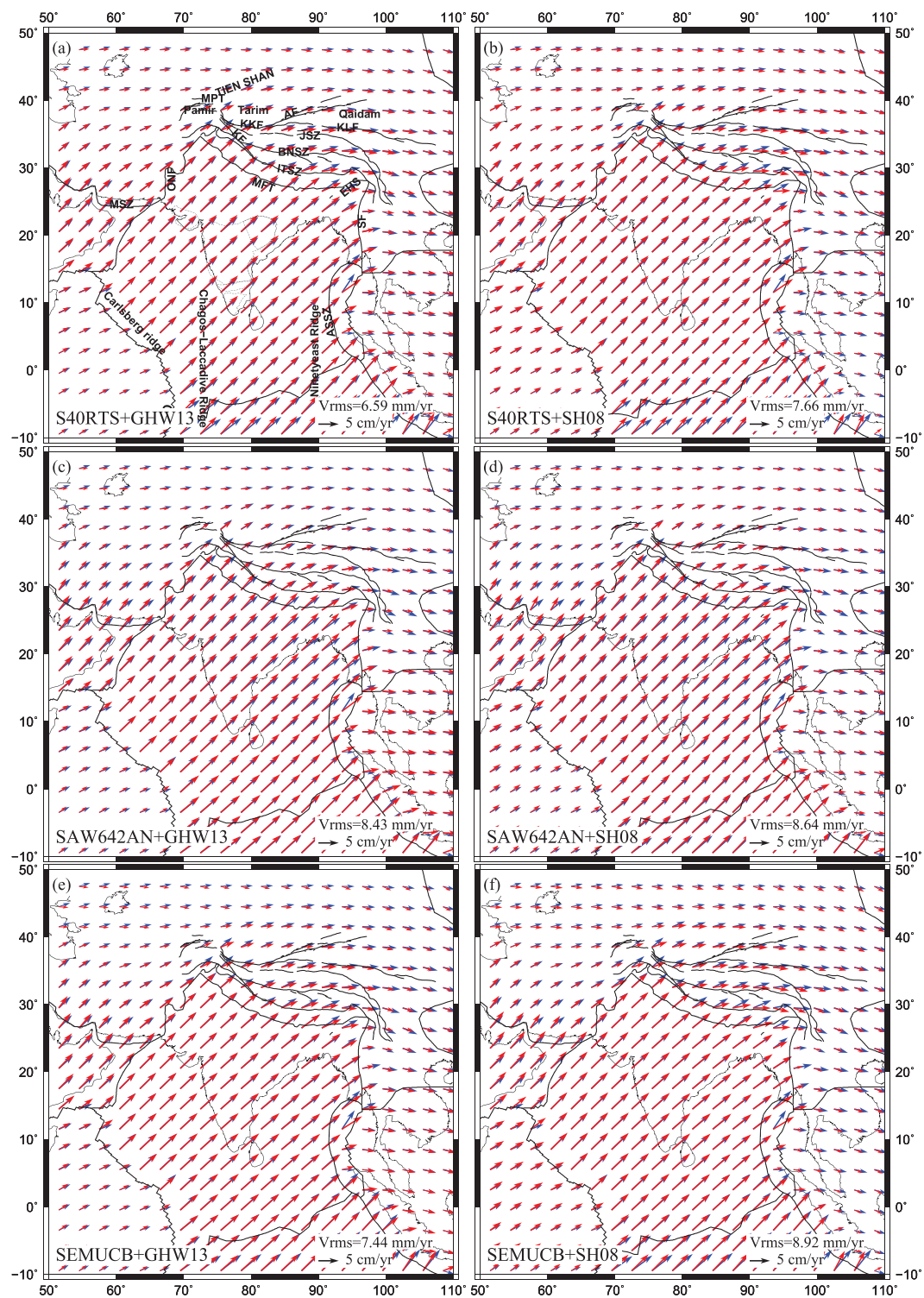


Figure 10. Plate velocities predicted using a combined model of gravitational potential energy and mantle tractions derived using density anomalies inferred from various tomography models for viscosity structures: GHW13 (a, c, e, g, i, and k) and SH08 (right panel). The red arrows denote the predicted velocities, and blue arrows indicate kinematic velocities (Kreemer et al., 2014), both in no-net-rotation frame. MFT = Main Frontal Thrust; MSZ = Makran Subduction Zone; MPT = Main Pamir Thrust; KKF = Karakax Fault; AF = Altyn Tagh fault; KF = Karakorum Fault; KLF = Kunlun Fault; JSZ = Jinshajiang Suture Zone; BNSZ = Bangong-Nujiang Suture Zone; ONF = Ornach-Nal Fault; EHS = Eastern Himalayan Syntaxis; SF = Sagaing Fault; ASSZ = Andaman Sumatra subduction zone; CIR = Central Indian Ridge.

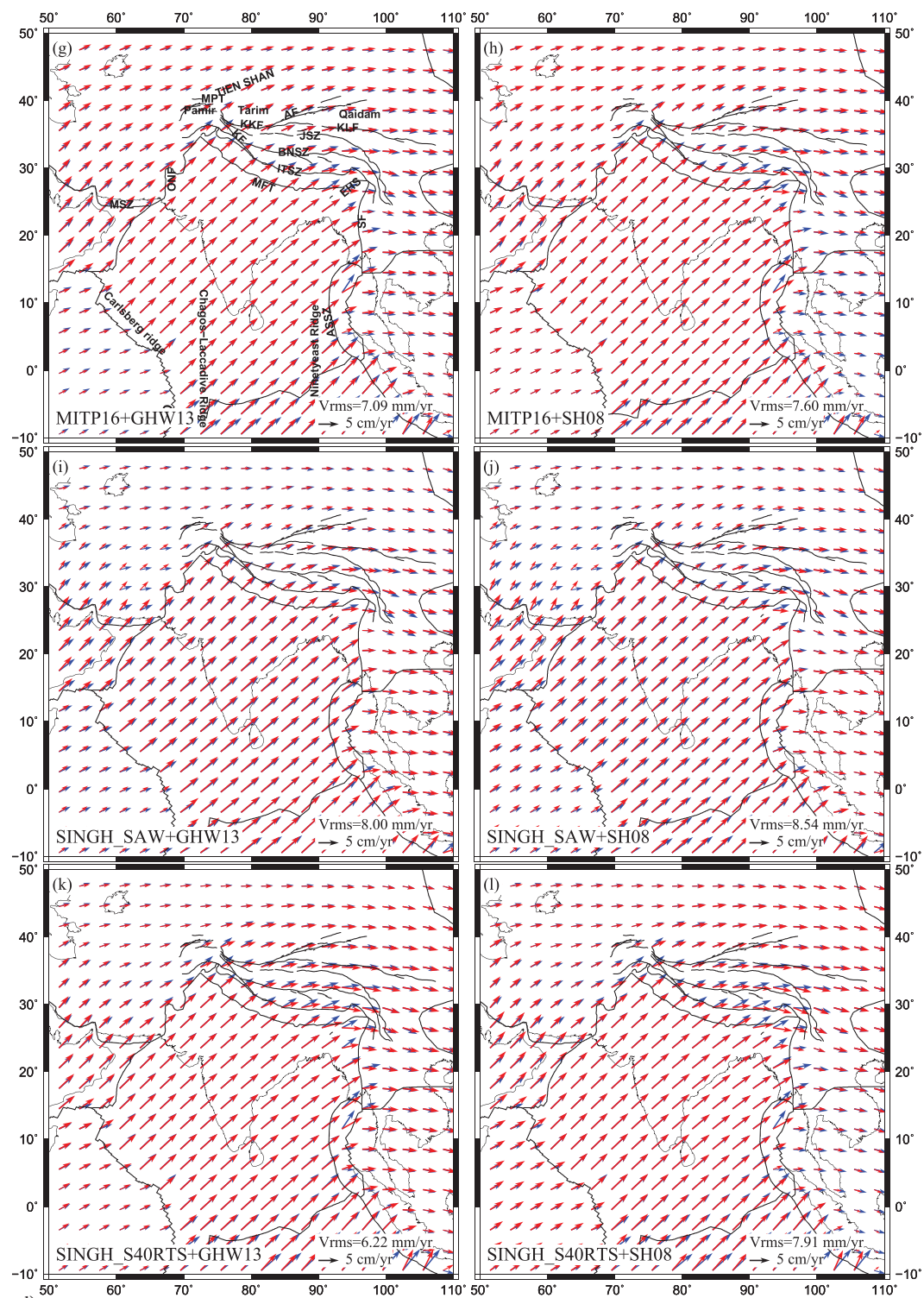


Figure 10. (continued)

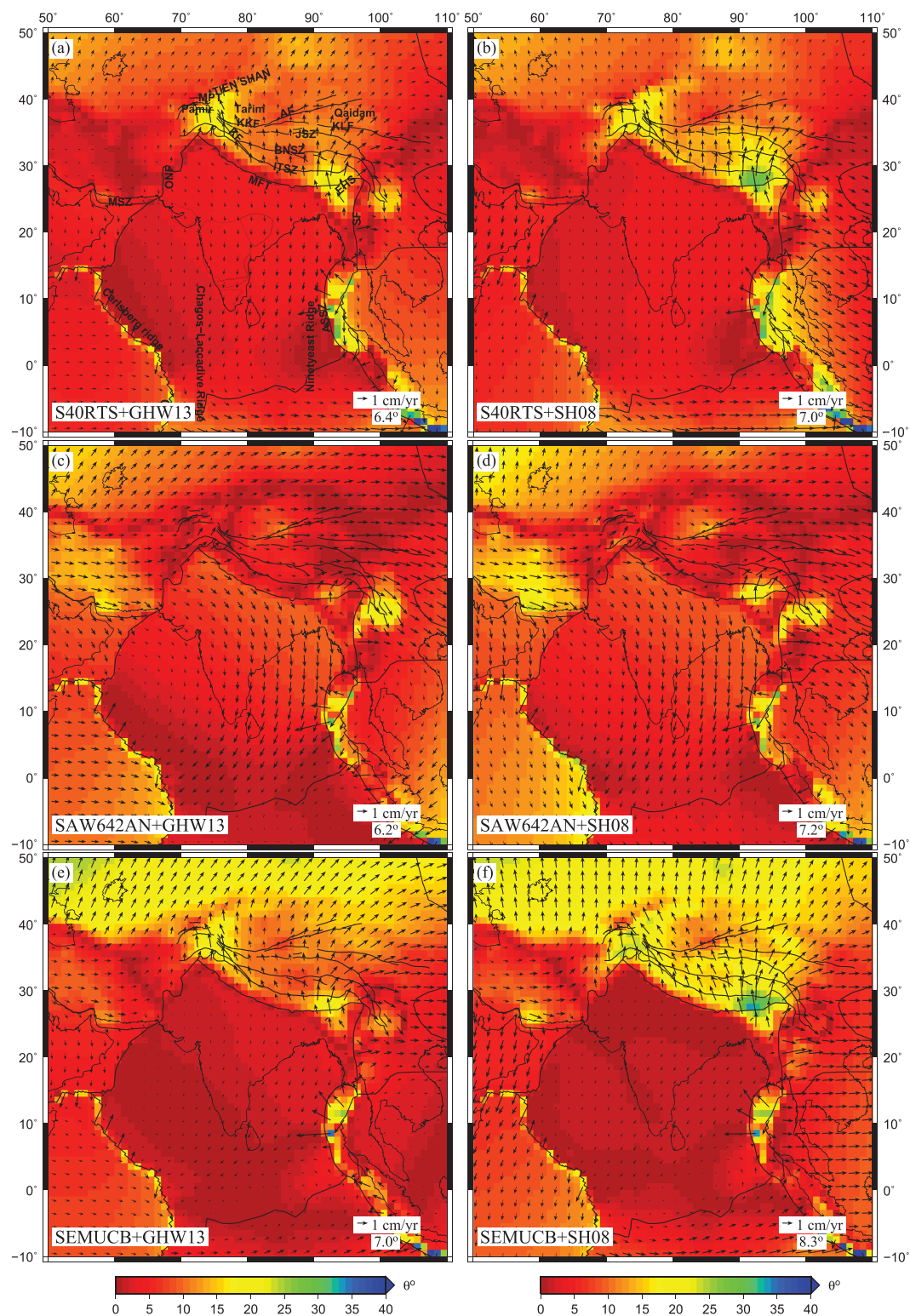


Figure 11. Angular misfit (θ) between kinematic velocities (Kreemer et al., 2014) and dynamic velocities predicted using a combined model of gravitational potential energy and mantle tractions derived from various tomography models with viscosity structures: GHW13 (a, c, e, g, i, and k) and SH08 (b, d, f, h, j, and l). The arrows show the vector difference between predicted and observed velocities with the average angular misfit shown in bottom right of each figure. MFT = Main Frontal Thrust; MSZ = Makran Subduction Zone; MPT = Main Pamir Thrust; KKF = Karakax Fault; AF = Altyn Tagh fault; KF = Karakorum Fault; KLF = Kunlun Fault; JSZ = Jinshajiang Suture Zone; BNSZ = Bangong-Nujiang Suture Zone; ONF = Ornach-Nal Fault; EHS = Eastern Himalayan Syntaxis; SF = Sagaing Fault; ASSZ = Andaman Sumatra subduction zone; CIR = Central Indian Ridge.

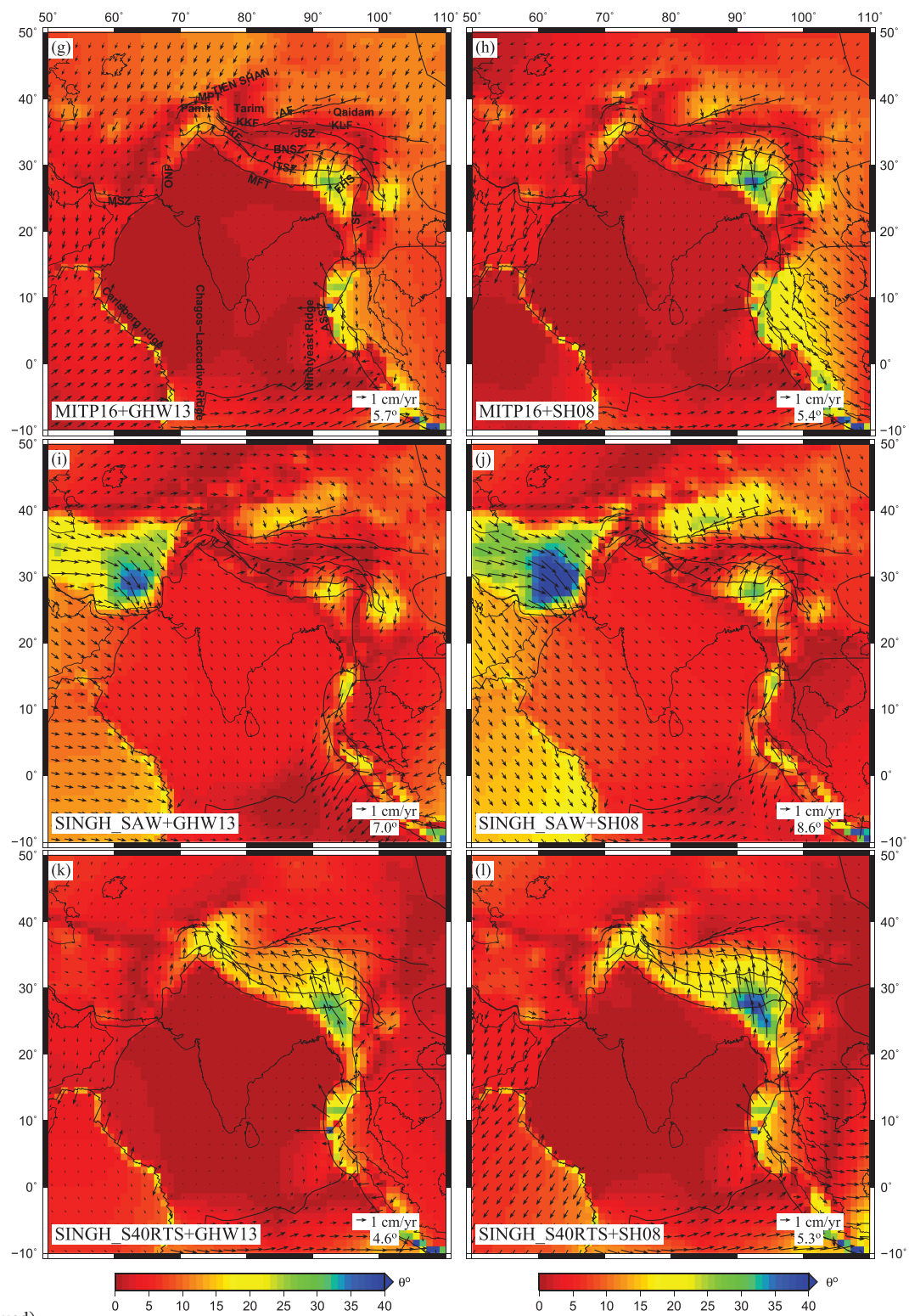


Figure 11. (continued)

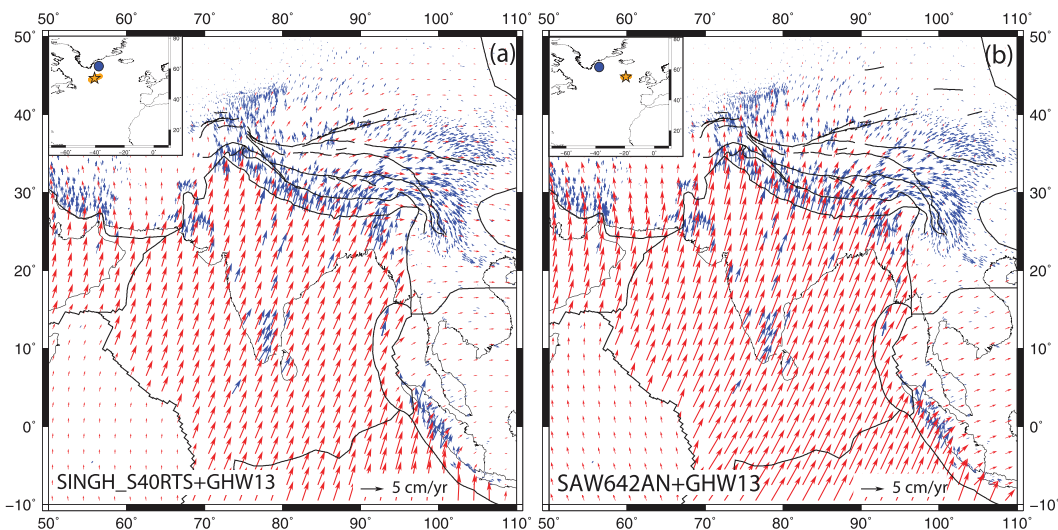


Figure 12. Comparison of observed GPS vectors (blue arrows) from Kreemer et al. (2014) and modeled velocities (red arrows) with respect to a fixed Eurasian plate from our global dynamic models: (a) combined SINGH_S40RTS+GHW13 and (b) SAW642AN+GHW13 models in a fixed Eurasian plate frame of reference. The inset figure shows the observed pole of rotation of the Indian plate (blue) from Kreemer et al. (2014) and the average pole of rotation of the Indian plate (orange star) predicted by combined SINGH_S40RTS+GHW13 and SAW642AN+GHW13 models.

The predicted plate velocities from the combined models are found to have smaller average RMS errors compared to the GPE-only case with significant improvements observed in the India-Eurasia collision zone (Figure 10). For all the models, there occurs a velocity mismatch in eastern Tibet close to the EHS where there is a 20–40° difference in the direction of velocity vectors as well as a difference in magnitude. A 2–3 cm northward component of velocity needs to be added to all the models, so that the predicted velocities match the observed ones in eastern Tibet (Figure 11). SAW642AN matches both the orientation and magnitude of the velocities within Tibet (Figures 11c and 11d), which is a remarkable improvement over GPE only model, whereas SEMUCB (Figures 11e and 11f) and SINGH_S40RTS (Figures 11k and 11l) are the worst in matching the kinematic velocities within Tibet. A degradation of fit is observed to the west of the collisional boundary for SINGH_SAW model. Within the Indian plate, the predicted dynamic velocities match the kinematic ones in both direction and magnitude for most models. The lowest RMS misfit (6.2 mm/year) and the lowest misfit (4.6°) is obtained for the SINGH_S40RTS model with the GHW13 viscosity structure (Figures 10k and 11k, respectively).

5. Discussion and Conclusion

The Indian plate is a complex region, defined by the continent-continent collision in the north. This has given rise to the highest topography on Earth and a seismically active region. The entire southern boundary is surrounded by the mid-oceanic ridges along with a very prominent diffuse oceanic deformation zone. The nondeforming region has also experienced some major intraplate earthquakes (Schulte-Pelkum et al., 2005). To understand the seismic hazard of the region, whether from the plate boundary earthquakes in the north or the intraplate earthquakes in the south, a thorough understanding of the deformation pattern of the lithosphere is required. Lack of such a comprehensive understanding stems from the paucity of data within the region as well as incompleteness of present deformation models. In recent years, higher resolution and more advanced crustal and tomography models have enabled a newer understanding of surface observations. The goal of the present study is to use some of the recent density and velocity models in an effort to understand the deformation of the Indian plate region as well as its surrounding deformation zones.

We use recent global tomography models such as S40RTS (Ritsema et al., 2011), SAW642AN (Mégnin & Romanowicz, 2000b), SEMUCB (French & Romanowicz, 2015), and MITP16 (Burdick et al., 2017), in addition to a regional P wave model (Singh et al., 2014), along with two radial viscosity structures, GHW13 (Ghosh et al., 2013), and SH08 (Steinberger & Holme, 2008), to drive instantaneous flow within the

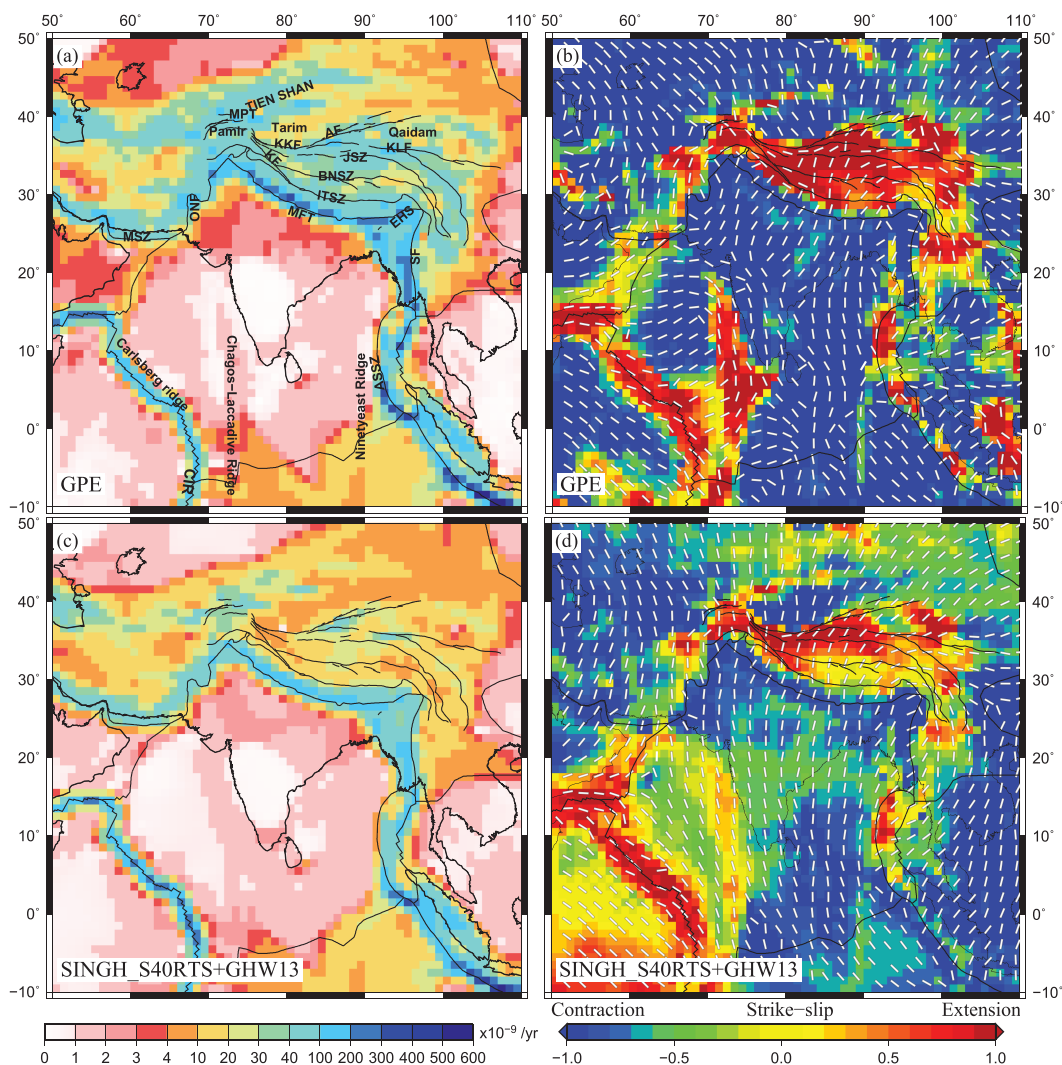


Figure 13. (and c) The second invariant of strain rates predicted by GPE only and SINGH_S40RTS combined models; (b and d) the principal strain axes directions from these models, plotted on a measure of the style of the strain rate tensor (refer to Figure 4b). MFT = Main Frontal Thrust; MSZ = Makran Subduction Zone; MPT = Main Pamir Thrust; KKF = Karakax Fault; AF = Altn Tagh fault; KF = Karakorum Fault; KLF = Kunlun Fault; JSZ = Jinshajiang Suture Zone; BNSZ = Bangong-Nujiang Suture Zone; ONF = Ornach-Nal Fault; EHS = Eastern Himalayan Syntaxis; SF = Sagaing Fault; ASSZ = Andaman Sumatra subduction zone; CIR = Central Indian Ridge; GPE = gravitational potential energy.

mantle using a convection code, HC (Hager & O'Connell, 1981). This convective flow gives rise to shear tractions that act at the base of the lithosphere FE model, which incorporates lateral viscosity variations, to yield deviatoric stresses. These stresses are then added to deviatoric stresses arising due to GPE variations within the lithosphere, calculated from the CRUST1.0 model, to obtain a total deviatoric stress field for the region. We use various surface observations as constraints, such as strain rates from the most recent version of the GSRM (Kreemer et al., 2014), plate velocities, SH_{\max} orientations and style of faulting from the WSM (Heidbach et al., 2016), to evaluate these models quantitatively. We see that in most cases, the addition of mantle tractions improve the fit to these constraints. We see that the SINGH_S40RTS model, which is a regional P wave model by Singh et al. (2014) embedded within S40RTS, a global S wave model, along with the GHW13 viscosity structure, provides the lowest misfit in all the cases. The improvement of fit to the observed deformation after adding the contribution from mantle tractions were shown earlier globally by Ghosh et al. (2008) and Ghosh et al. (2013). Wang et al. (2015) also showed that S40RTS and SAW642AN tomography models were quite effective in matching various surface observations globally.

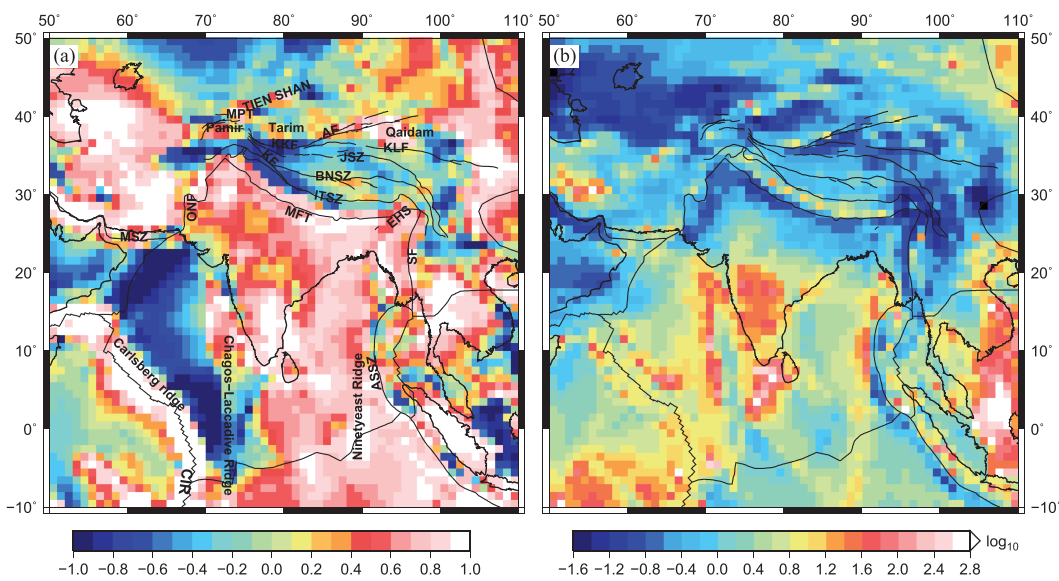


Figure 14. Comparison of the predicted deviatoric stresses from GPE and mantle tractions alone for the SINGH_S40RTS model with GHW13 viscosity structure model. (a) Correlation coefficients (r) between the deviatoric stress tensors predicted from GPE and mantle tractions. (b) The ratio of the second invariant of deviatoric stresses (T/T) predicted using mantle tractions and GPE. MFT = Main Frontal Thrust; MSZ = Makran Subduction Zone; MPT = Main Pamir Thrust; KKF = Karakax Fault; AF = Altyn Tagh fault; KF = Karakorum Fault; KLF = Kunlun Fault; JSZ = Jinshajiang Suture Zone; BNSZ = Bangong-Nujiang Suture Zone; ONF = Ornach-Nal Fault; EHS = Eastern Himalayan Syntaxis; SF = Sagaing Fault; ASSZ = Andaman Sumatra subduction zone; CIR = Central Indian Ridge; GPE = gravitational potential energy.

We also calculate a total error given by

$$\text{Total Error} = 1 - \text{Corr}_{\text{GSRM}} + \log(V_{\text{rms}}) + \epsilon_p \quad (8)$$

(Wang et al., 2015) that takes into account misfit from all constraints. Here, $\text{Corr}_{\text{GSRM}}$ is the average correlation obtained using equation (7), V_{rms} is the RMS error between the predicted and observed plate velocities and ϵ_p is the total misfit between predicted and observed SH_{max} , which had been defined previously in section 3. The values obtained for all models are summarized in Table 1. GPE shows the highest total error (>2), while the lowest error (~ 1.51) is obtained for combined SINGH_S40RTS model with GHW13. S40RTS too shows a low total error, quite similar to that obtained for SINGH_S40RTS for GHW13 viscosity structure. We next take our best model (SINGH_S40RTS+GHW13) and compare the predicted velocities with the actual GPS velocities in a fixed Eurasian frame of reference (Figure 12a). We see that except for Tibet, the predicted velocities match the observed ones quite well, both in direction and magnitude. In eastern Tibet, our model predicts a more eastward component of velocity compared to the observed northeasterly one. While SINGH_S40RTS predicts velocities that poorly match the observed velocities in Tibet, velocities predicted from SAW642AN show a lot lower misfit compared to the other models (Figure 11c). Hence, we also compare velocities from SAW642AN in a fixed Eurasian frame of reference with GPS velocities (Figure 12b). We observe a significant improvement in eastern Tibet as the predicted velocities show a north-easterly movement of the Indian plate with respect to the Eurasian plate which is in accordance with observed GPS velocities. In fact, SAW642AN model shows a better fit to observed GPS velocities in entire Tibet as compared to SINGH_S40RTS model.

We also calculate the second invariants of strain rate from GPE only and SINGH_S40RTS+GHW13 models (Figures 13a and 13c). Both models show no deformation within the Indian craton and negligible deformation within the other intraplate areas in accordance with an earlier study (cf. Paul et al., 2001), indicating high plateness predicted by these models. The highest strain rates occur in the India-Eurasia collision zone for GPE only model (Figure 13a), while SINGH_S40RTS model shows much lower strain rates there (Figure 13c). We also predict principal axes and regime of faulting in the study area by using these strain rates (Figures 13b and 13d; cf. Figure 4b). Significant differences between the models are observed in Tibet. GPE model shows a purely extensional regime, while addition of compressional stresses from

mantle tractions leads to introduction of strike-slip type of deformation in this area for SINGH_S40RTS +GHW13. Large extension is predicted along the Carlsberg ridge by both models. GPE only model shows pure extension along Chagos-Laccadive Ridge, whereas SINGH_S40RTS+GHW13 model predicts strike-slip style of faulting in this area. The predicted stress/strain directions from these two models are also different in the Arabian Sea. Major compression is observed in the eastern Indian ocean, IAP and along the India-Eurasia collision boundary by both models.

We compare the predicted deviatoric stresses from GPE and mantle sources for our best model (SINGH_S40RTS) in order to quantitatively assess the dominant source of deformation (Figure 14). We compute a correlation coefficient (r) given by, $r=\tau\cdot\tau'/T^*T'$ (Ghosh et al., 2013) to constrain the similarity in the style and orientation of predicted stresses. Here, τ denotes the components of deviatoric stress from GPE and τ' indicates the components of deviatoric stresses from mantle tractions alone (SINGH_S40RTS with GHW13 viscosity structure), while T and T' are the second invariants of deviatoric stresses from GPE and mantle tractions alone respectively, and $*$ represents simple multiplication; $\tau\cdot\tau'$ is given by

$$\tau\cdot\tau' = 2\tau_{\phi\phi}\tau'_{\phi\phi} + 2\tau_{\theta\theta}\tau'_{\theta\theta} + 2\tau_{\phi\theta}\tau'_{\phi\theta} + \tau_{\phi\phi}\tau'_{\theta\theta} + \tau_{\theta\theta}\tau'_{\phi\phi} \quad (9)$$

as per Ghosh et al. (2013). A high correlation suggests that both GPE and mantle sources predict similar type of stresses as observed in the Bay of Bengal as well as within mainland India. Very similar style of GPE and mantle derived stresses are also observed in IAP and along the Carlsberg ridge (Figure 14a). However, the correlation becomes negative in the western Indian Ocean and Arabian Sea, suggesting that stresses predicted by GPE and mantle tractions are anticorrelated in style and/or orientation. We also observe anticorrelation in the western Himalayas and Tibet, while correlation improves somewhat in central Tibet. The ratio between the second invariants of stresses predicted by mantle tractions alone from SINGH_S40RTS +GHW13 and GPE is observed to be low along the India-Eurasia collision boundary, EHS as well as in eastern Tibet, which suggests dominance of GPE-derived sources over mantle derived sources in those areas (Figure 14b). One of the reasons for not fitting observed velocities well within Tibet could be due to a much smaller contribution from mantle tractions for the SINGH_S40RTS model in those areas. However, a prominent contribution from mantle sources as compared to GPE is observed in a large part of the Indian plate, especially in the southern peninsula as evident by the high ratio in those regions.

We show that lithosphere buoyancy forces coupled with density-driven mantle convection are largely able to explain the deformation of the Indian plate and the northern collisional zone. With the advent of higher resolution crustal and tomography models, more GPS measurements and greater data coverage, the predictions from the dynamic models are approaching a level of accuracy that can match the uncertainty in the kinematic models themselves. Flesch et al. (2018) had argued about the inadequacy of surface velocities in the India-Eurasia collision zone for constraining its dynamics. Hence, additional constraints, such as stresses, geoid anomalies and topography could be important for a complete understanding of the dynamics. A clear understanding of both intraplate and interplate dynamics will be crucial to address questions related to seismicity patterns and seismic hazard in this region.

Acknowledgments

Figures were prepared using GMT 4.5.11 by P. Wessel and W. F. Smith. S. Singh was funded by UGC Grant F. 2-99/1998(SA-I). Comments from two anonymous reviewers considerably improved the manuscript. The tomography models used in our study can be accessed as follows: SAW642AN on IRIS website (<https://ds.iris.edu/ds/products/emc-earthmodels/>), S40RTS on <http://jrtsema.earth.lsa.umich.edu//Research.html> website, SEMUCB-WM1 on http://seismo.berkeley.edu/wiki_br/Main_Page and MITP_2016MAY from the electronic supplement to the article by Burdick et al. (2017).

References

- Artyushkov, E. V. (1973). Stresses in the lithosphere caused by crustal thickness inhomogeneities. *Journal of Geophysical Research*, 78(32), 7675–7708.
- Avouac, J. P., & Tapponnier, P. (1993). Kinematic model of active deformation in central Asia. *Geophysical Research Letters*, 20(10), 895–898.
- Bai, W., Vigny, C., Ricard, Y., & Froidevaux, C. (1992). On the origin of deviatoric stresses in the lithosphere. *Journal of Geophysical Research*, 97(B8), 11,729–11,737.
- Banerjee, P., Bürgmann, R., Nagarajan, B., & Apel, E. (2008). Intraplate deformation of the Indian subcontinent. *Geophysical Research Letters*, 35, L18301. <https://doi.org/10.1029/2008GL035468>
- Bhatia, S. C., Kumar, M. R., & Gupta, H. K. (1999). A probabilistic seismic hazard map of India and adjoining regions. *Annali di Geofisica*, 42(6), 1153–1164.
- Bilham, R., Larson, K., & Freymueller, J. (1997). Gps measurements of present-day convergence across the nepal himalaya. *Nature*, 386(6620), 61–64.
- Bird, P. (1998). Testing hypotheses on plate-driving mechanisms with global lithosphere models including topography, thermal structure, and faults. *Journal of Geophysical Research*, 103(B5), 10,115–10,129.
- Bird, P., Liu, Z., & Rucker, W. K. (2008). Stresses that drive the plates from below: Definitions, computational path, model optimization, and error analysis. *Journal of Geophysical Research*, 113, B11406. <https://doi.org/10.1029/2007JB005460>
- Biswas, S. (1989). State of stress and its bearing on tectonics under the Tibetan Plateau. *Physics of the Earth and Planetary Interiors*, 54(1–2), 4–9.

- Burdick, S., Chang, L., Martynov, V., Cox, T., Eakins, J., Mulder, T., et al. (2017). Model update may 2016: Upper-mantle heterogeneity beneath North America from travel-time tomography with global and usarray data. *Seismological Research Letters*, 88(2A), 319–325.
- Calais, E., Dong, L., Wang, M., Shen, Z., & Vergnolle, M. (2006). Continental deformation in Asia from a combined GPS solution. *Geophysical Research Letters*, 33, L24319. <https://doi.org/10.1029/2006GL028433>
- Cande, S. C., & Stegman, D. R. (2011). Indian and African plate motions driven by the push force of the Réunion plume head. *Nature*, 475(7354), 47–52.
- Chen, Z. H., Burchfiel, B. C., Liu, Y., King, R. W., Royden, L. H., Tang, W., et al. (2000). Global Positioning System measurements from eastern Tibet and their implications for India/Eurasia intercontinental deformation. *Journal of Geophysical Research*, 105(B7), 16,215–16,227.
- Coblenz, D., Richardson, R. M., & Sandiford, M. (1994). On the gravitational potential of the Earth's lithosphere. *Tectonics*, 13(4), 929–945.
- Copley, A., Avouac, J. P., & Royer, J. Y. (2010). India-Asia collision and the Cenozoic slowdown of the Indian plate: Implications for the forces driving plate motions. *Journal of Geophysical Research*, 115, B03410. <https://doi.org/10.1029/2009JB006634>
- Curry, J. R., & Munasinghe, T. (1989). Timing of intraplate deformation, northeastern Indian Ocean. *Earth and Planetary Science Letters*, 94(1–2), 71–77.
- DeMets, C., Gordon, R. G., Argus, D., & Stein, S. (1990). Current plate motions. *Geophysical Journal International*, 101(2), 425–478.
- England, P., & Houseman, G. (1986). Finite strain calculations of continental deformation: 2. Comparison with the India-Asia collision zone. *Journal of Geophysical Research*, 91(B3), 3664–3676.
- England, P., & Houseman, G. (1989). Extension during continental convergence, with application to the Tibetan Plateau. *Journal of Geophysical Research*, 94(B12), 17561–17579.
- England, P., & McKenzie, D. (1982). A thin viscous sheet model for continental deformation. *Geophysical Journal International*, 70(2), 295–321.
- England, P., & McKenzie, D. (1983). Correction to: A thin viscous sheet model for continental deformation. *Geophysical Journal International*, 73(2), 523–532.
- England, P., & Molnar, P. (1997). Active deformation of Asia: From kinematics to dynamics. *Science*, 278(5338), 647–650.
- England, P., & Molnar, P. (2005). Late Quaternary to decadal velocity fields in Asia. *Journal of Geophysical Research*, 110, B12401. <https://doi.org/10.1029/2004JB003541>
- Finzel, E. S., Flesch, L. M., Ridgway, K. D., Holt, W. E., & Ghosh, A. (2015). Surface motions and intraplate continental deformation in Alaska driven by mantle flow. *Geophysical Research Letters*, 42, 4350–4358. <https://doi.org/10.1002/2015GL063987>
- Fleitout, L., & Froidevaux, C. (1982). Tectonics and topography for a lithosphere containing density heterogeneities. *Tectonics*, 1(1), 21–56.
- Fleitout, L., & Froidevaux, C. (1983). Tectonic stresses in the lithosphere. *Tectonics*, 2(3), 315–324.
- Flesch, L. M., Bendick, R., & Bischoff, S. (2018). Limitations on inferring 3D architecture and dynamics from surface velocities in the india-eurasia collision zone. *Geophysical Research Letters*, 45, 1379–1386. <https://doi.org/10.1002/2017GL076503>
- Flesch, L. M., Haines, A. J., & Holt, W. E. (2001). Dynamics of the India-Eurasia collision zone. *Journal of Geophysical Research*, 106(B8), 16,435–16,460.
- Flesch, L. M., Holt, W. E., Haines, A. J., Wen, L., & Shen-Tu, B. (2007). The dynamics of western North America: Stress magnitudes and the relative role of gravitational potential energy, plate interaction at the boundary and basal tractions. *Geophysical Journal International*, 169(3), 866–896.
- Flesch, L. M., & Kreemer, C. (2010). Gravitational potential energy and regional stress and strain rate fields for continental plateaus: Examples from the central andes and colorado plateau. *Tectonophysics*, 482(1–4), 182–192.
- Forte, A. M., Quéré, S., Moucha, R., Simmons, N. A., Grand, S. P., Mitrovica, J. X., & Rowley, D. B. (2010). Joint seismic-geodynamic-mineral physical modelling of African geodynamics: A reconciliation of deep-mantle convection with surface geophysical constraints. *Earth and Planetary Science Letters*, 295(3), 329–341.
- Frank, F. C. (1972). Plate tectonics, the analogy with glacier flow, and isostasy, *Flow and fracture of rocks* pp. 285–292). Washington, D. C: AGU.
- French, S. W., & Romanowicz, B. (2015). Broad plumes rooted at the base of the Earth's mantle beneath major hotspots. *Nature*, 525(7567), 95–99.
- Ghosh, A., Becker, T. W., & Humphreys, E. D. (2013). Dynamics of the North American continent. *Geophysical Journal International*, 194(2), 651–669.
- Ghosh, A., & Holt, W. E. (2012). Plate motions and stresses from global dynamic models. *Science*, 335(6070), 838–843.
- Ghosh, A., Holt, W. E., & Bahadori, A. (2019). Role of large scale tectonic forces in intraplate earthquakes of Central and Eastern North America. *Geochemistry, Geophysics, Geosystems*, 20, 2134–2156. <https://doi.org/10.1029/2018GC008060>
- Ghosh, A., Holt, W. E., & Flesch, L. M. (2009). Contribution of gravitational potential energy differences to the global stress field. *Geophysical Journal International*, 179(2), 787–812.
- Ghosh, A., Holt, W. E., Flesch, L. M., & Haines, A. J. (2006). Gravitational potential energy of the Tibetan Plateau and the forces driving the Indian plate. *Geology*, 34(5), 321–324.
- Ghosh, A., Holt, W. E., & Wen, L. (2013). Predicting the lithospheric stress field and plate motions by joint modeling of lithosphere and mantle dynamics. *Journal of Geophysical Research: Solid Earth*, 118, 346–368. <https://doi.org/10.1029/2012JB009516>
- Ghosh, A., Holt, W. E., Wen, L., Haines, A. J., & Flesch, L. M. (2008). Joint modeling of lithosphere and mantle dynamics elucidating lithosphere-mantle coupling. *Geophysical Research Letters*, 35, L16309. <https://doi.org/10.1029/2008GL034365>
- Hager, B. H., & O'Connell, R. J. (1981). A simple global model of plate dynamics and mantle convection. *Journal of Geophysical Research*, 86(B6), 4843–4867.
- Heidbach, O., Rajabi, M., Reiter, K., & Ziegler, M. (2016). WSM Team (2016): World Stress Map Database Release 2016. GFZ Data Services <http://doi.org/10.5880/WSM.2016.001>
- Hirschberg, H. P., Lamb, S., & Savage, M. K. (2018). Strength of an obliquely convergent plate boundary: Lithospheric stress magnitudes and viscosity in New Zealand. *Geophysical Journal International*, 216(2), 1005–1024.
- Holt, W. E. (2000). Correlated crust and mantle strain fields in Tibet. *Geology*, 28(1), 67–70.
- Holt, W. E., Li, M., & Haines, A. J. (1995). Earthquake strain rates and instantaneous relative motions within central and eastern Asia. *Geophysical Journal International*, 122(2), 569–593.
- Holt, W. E., Ni, J. F., Wallace, T. C., & Haines, A. J. (1991). The active tectonics of the eastern Himalayan syntaxis and surrounding regions. *Journal of Geophysical Research*, 96(B9), 14,595–14,632.
- Houseman, G., & England, P. (1986). A dynamical model of lithosphere extension and sedimentary basin formation. *Journal of Geophysical Research*, 91(B1), 719–729.

- Houseman, G., & England, P. (1993). Crustal thickening versus lateral expulsion in the Indian-Asian continental collision. *Journal of Geophysical Research*, 98(B7), 12,233–12,249.
- Huang, M. H., Bürgmann, R., & Freed, A. M. (2014). Probing the lithospheric rheology across the eastern margin of the Tibetan Plateau. *Earth and Planetary Science Letters*, 396, 88–96.
- Husson, L., & Ricard, Y. (2004). Stress balance above subduction: Application to the Andes. *Earth and Planetary Science Letters*, 222(3-4), 1037–1050.
- Iaffaldano, G., Bodin, T., & Cambridge, M. (2013). Slow-downs and speed-ups of India-Eurasia convergence since 20 Ma: Data-noise, uncertainties and dynamic implications. *Earth and Planetary Science Letters*, 367, 146–156.
- Iaffaldano, G., Bunge, H. P., & Dixon, T. H. (2006). Feedback between mountain belt growth and plate convergence. *Geology*, 34(10), 893–896.
- Iaffaldano, G., Davies, D. R., & DeMets, C. (2018). Indian Ocean floor deformation induced by the Reunion plume rather than the Tibetan Plateau. *Nature Geoscience*, 11, 362–366.
- Jay, C. N., Flesch, L. M., & Bendick, R. O. (2017). Kinematics and dynamics of the Pamir, Central Asia: Quantifying surface deformation and force balance in an intracontinental subduction zone. *Journal of Geophysical Research: Solid Earth*, 122, 4741–4762. <https://doi.org/10.1029/2017JB014177>
- Jay, C. N., Flesch, L. M., & Bendick, R. O. (2018). Kinematics and dynamics of the Pamir, Central Asia: Quantifying the roles of continental subduction in force balance. *Journal of Geophysical Research: Solid Earth*, 123, 8161–8179. <https://doi.org/10.1029/2018JB015615>
- Khattri, K., Rogers, A., Perkins, D., & Algermissen, S. (1984). A seismic hazard map of India and adjacent areas. *Tectonophysics*, 108(1-2), 93–134.
- Khattri, K., & Tyagi, A. (1983). Seismicity patterns in the Himalayan plate boundary and identification of the areas of high seismic potential. *Tectonophysics*, 96(3-4), 281–297.
- Klein, E. C., Flesch, L. M., Holt, W. E., & Haines, A. J. (2009). Evidence of long-term weakness on seismogenic faults in western North America from dynamic modeling. *Journal of Geophysical Research*, 114, B03402. <https://doi.org/10.1029/2007JB005201>
- Kong, X., & Bird, P. (1995). SHELLS: A thin-shell program for modeling neotectonics of regional or global lithosphere with faults. *Journal of Geophysical Research*, 100(B11), 22,129–22,131.
- Kreemer, C., Blewitt, G., & Klein, E. C. (2014). A geodetic plate motion and Global Strain Rate Model. *Geochemistry, Geophysics, Geosystems*, 15, 3849–3889. <https://doi.org/10.1002/2014GC005407>
- Larson, K. M., Bürgmann, R., Bilham, R., & Freymueller, J. T. (1999). Kinematics of the India-Eurasia collision zone from GPS measurements. *Journal of Geophysical Research*, 104(B1), 1077–1093.
- Laske, G., Masters, G., Ma, Z., & Pasyanos, M. (2013). Update on CRUST1.0—A 1-degree global model of Earth's crust. *Geophysical Research Abstracts*, 15, 2658.
- Lawrence, R., Yeats, R., Khan, S., Farah, A., & DeJong, K. (1981). Thrust and strike slip fault interaction along the Chaman transform zone, Pakistan. *Geological Society, London, Special Publications*, 9(1), 363–370.
- Lithgow-Bertelloni, C., & Guynn, J. H. (2004). Origin of the lithospheric stress field. *Journal of Geophysical Research*, 109, B01408. <https://doi.org/10.1029/2003JB002467>
- Liu, C. S., Curraj, J. R., & McDonald, J. M. (1983). New constraints on the tectonic evolution of the eastern Indian ocean. *Earth and Planetary Science Letters*, 65(2), 331–342.
- Matte, P., Tapponnier, P., Arnaud, N., Bourjot, L., Avouac, J. P., Vidal, P., et al. (1996). Tectonics of western Tibet, between the Tarim and the Indus. *Earth and Planetary Science Letters*, 142(3-4), 311–330.
- Mégnin, C., & Romanowicz, B. (2000a). The shear velocity structure of the mantle from the inversion of body, surface and higher modes waveforms. *Geophysical Journal International*, 143, 709–728.
- Mégnin, C., & Romanowicz, B. (2000b). The three-dimensional shear velocity structure of the mantle from the inversion of body, surface and higher-mode waveforms. *Geophysical Journal International*, 143(3), 709–728.
- Merkouriev, S., & DeMets, C. (2006). Constraints on Indian plate motion since 20 Ma from dense Russian magnetic data: Implications for Indian plate dynamics. *Geochemistry, Geophysics, Geosystems*, 7, Q02002. <https://doi.org/10.1029/2005GC001079>
- Milner, K., Becker, T. W., Boschi, L., Sain, J., Schorlemmer, D., & Waterhouse, H. (2009). New software framework to share research tools. *Eos, Transactions American Geophysical Union*, 90(12), 104–104.
- Molnar, P., England, P., & Martinod, J. (1993). Mantle dynamics, uplift of the Tibetan Plateau, and the Indian monsoon. *Reviews of Geophysics*, 31(4), 357–396.
- Molnar, P., Fitch, T. J., & Wu, F. T. (1973). Fault plane solutions of shallow earthquakes and contemporary tectonics in Asia. *Earth and Planetary Science Letters*, 19(2), 101–112.
- Molnar, P., & Stock, J. M. (2009). Slowing of India's convergence with Eurasia since 20 Ma and its implications for Tibetan mantle dynamics. *Tectonics*, 28, TC3001. <https://doi.org/10.1029/2008TC002271>
- Molnar, P., & Tapponnier, P. (1975). Cenozoic tectonics of Asia: Effects of a continental collision. *Science*, 189(4201), 419–426.
- Molnar, P., & Tapponnier, P. (1978). Active tectonics of Tibet. *Journal of Geophysical Research*, 83(B11), 5361–5375.
- Morgan, W. J. (1968). Rises, trenches, great faults, and crustal blocks. *Journal of Geophysical Research*, 73(6), 1959–1982.
- Morgan, W. J. (1972). Deep mantle convection plumes and plate motions. *AAPG bulletin*, 56(2), 203–213.
- Naliboff, J. B., Lithgow-Bertelloni, C., Ruff, L. J., & de Koker, N. (2012). The effects of lithospheric thickness and density structure on Earth's stress field. *Geophysical Journal International*, 188(1), 1–17.
- Nataf, H. C., & Ricard, Y. (1996). 3SMAC: An a priori tomographic model of the upper mantle based on geophysical modeling. *Physics of the Earth and Planetary Interiors*, 95(1-2), 101–122.
- Ni, J., & Barazangi, M. (1985). Active tectonics of the western Tethyan Himalaya above the underthrusting Indian Plate: The Upper Sutlej River Basin as a pull-apart structure. *Tectonophysics*, 112(1-4), 277–295.
- Parvez, I. A., Vaccari, F., & Panza, G. F. (2003). A deterministic seismic hazard map of India and adjacent areas. *Geophysical Journal International*, 155(2), 489–508.
- Patriat, P., & Achache, J. (1984). India-Eurasia collision chronology has implications for crustal shortening and driving mechanism of plates. *Nature*, 311(5987), 615–621.
- Paul, J., Bürgmann, R., Gaur, V. K., Bilham, R., Larson, K. M., Ananda, M. B., et al. (2001). The motion and active deformation of India. *Geophysical Research Letters*, 28(4), 647–650.
- Peltzer, G., & Saucier, F. (1996). Present-day kinematics of Asia derived from geologic fault rates. *Journal of Geophysical Research*, 101(B12), 27,943–27,956.

- Peltzer, G., & Tapponnier, P. (1988). Formation and evolution of strike-slip faults, rifts, and basins during the India-Asia collision: An experimental approach. *Journal of Geophysical Research*, 93(B12), 15,085–15,117.
- Ratschbacher, L., Frisch, W., Liu, G., & Chen, C. (1994). Distributed deformation in southern and western Tibet during and after the India-Asia collision. *Journal of Geophysical Research*, 99(B10), 19,917–19,945.
- Richardson, R. M. (1992). Ridge forces, absolute plate motions, and the intraplate stress field. *Journal of Geophysical Research*, 97(B8), 11,739–11,748.
- Richardson, R. M., Solomon, S. C., & Sleep, N. H. (1979). Tectonic stress in the plates. *Reviews of Geophysics*, 17(5), 981–1019.
- Ritsema, J., Deuss, A. A., Van Heijst, H. J., & Woodhouse, J. H. (2011). S40RTS: A degree-40 shear-velocity model for the mantle from new Rayleigh wave dispersion, teleseismic traveltimes and normal-mode splitting function measurements. *Geophysical Journal International*, 184(3), 1223–1236.
- Ryder, I., Parsons, B., Wright, T. J., & Funning, G. J. (2007). Post-seismic motion following the 1997 Manyi (Tibet) earthquake: InSAR observations and modelling. *Geophysical Journal International*, 169(3), 1009–1027.
- Sandiford, M., & Coblenz, D. (1994). Plate-scale potential-energy distributions and the fragmentation of ageing plates. *Earth and Planetary Science Letters*, 126(1–3), 143–159.
- Schulte-Pelkum, V., Monsalve, G., Sheehan, A., Pandey, M. R., Sapkota, S., Bilham, R., & Wu, F. (2005). Imaging the Indian subcontinent beneath the himalaya. *Nature*, 435(7046), 1222–1225.
- Shen, Z. K., Lü, J., Wang, M., & Bürgmann, R. (2005). Contemporary crustal deformation around the southeast borderland of the Tibetan Plateau. *Journal of Geophysical Research*, 110, B11409. <https://doi.org/10.1029/2004JB003421>
- Singh, S., Agrawal, S., & Ghosh, A. (2017). Understanding deep Earth dynamics: A numerical modelling approach. *Current Science*, 112(7), 1463–1473.
- Singh, A., Mercier, J. P., Ravi Kumar, M., Srinagesh, D., & Chadha, R. K. (2014). Continental scale body wave tomography of India: Evidence for attrition and preservation of lithospheric roots. *Geochemistry, Geophysics, Geosystems*, 15, 658–675. <https://doi.org/10.1002/2013GC005056>
- Steinberger, B., & Holme, R. (2008). Mantle flow models with core-mantle boundary constraints and chemical heterogeneities in the lowermost mantle. *Journal of Geophysical Research*, 113, B05403. <https://doi.org/10.1029/2007JB005080>
- Steinberger, B., Schmeling, H., & Marquart, G. (2001). Large-scale lithospheric stress field and topography induced by global mantle circulation. *Earth and Planetary Science Letters*, 186(1), 75–91.
- Stotz, I. L., Iaffaldano, G., & Davies, D. R. (2017). Late Miocene Pacific plate kinematic change explained with coupled global models of mantle and lithosphere dynamics. *Geophysical Research Letters*, 44, 7177–7186.
- Tapponnier, P., & Molnar, P. (1979). Active faulting and Cenozoic tectonics of the Tien Shan, Mongolia, and Baykal regions. *Journal of Geophysical Research*, 84(B7), 3425–3459.
- Tapponnier, P., Peltzer, G., Le Dain, A. Y., Armijo, R., & Cobbold, P. (1982). Propagating extrusion tectonics in Asia: New insights from simple experiments with plasticine. *Geology*, 10(12), 611–616.
- van Hinsbergen, D. J. J., Steinberger, B., Doubrovine, P. V., & Gassmöller, R. (2011). Acceleration and deceleration of India-Asia convergence since the cretaceous: Roles of mantle plumes and continental collision. *Journal of Geophysical Research*, 116, B06101. <https://doi.org/10.1029/2010JB008051>
- Vergnolle, M., Calais, E., & Dong, L. (2007). Dynamics of continental deformation in asia. *Journal of Geophysical Research*, 112, B11403. <https://doi.org/10.1029/2006JB004807>
- Wang, X., Holt, W. E., & Ghosh, A. (2015). Joint modeling of lithosphere and mantle dynamics: Evaluation of constraints from global tomography models. *Journal of Geophysical Research: Solid Earth*, 120, 8633–8655.
- Wang, X., Holt, W. E., & Ghosh, A. (2019). Joint modeling of lithosphere and mantle dynamics: Sensitivity to viscosities within the lithosphere, asthenosphere, transition zone, and D'' layers. *Physics of the Earth and Planetary Interiors*, 293, <https://doi.org/10.1016/j.pepi.2019.05.006>
- Weissel, J. K., Anderson, R. N., & Geller, C. A. (1980). Deformation of the Indo-Australian plate. *Nature*, 287(5780), 284–291.
- Wilson, J. T. (1965). A new class of faults and their bearing on continental drift. *Nature*, 207(4995), 343–347.
- Zhang, P. Z., Shen, Z., Wang, M., Gan, W., Burgmann, R., Molnar, P., et al. (2004). Continuous deformation of the Tibetan Plateau from global positioning system data. *Geology*, 32(9), 809–812.
- Zheng, G., Wang, H., Wright, T. J., Lou, Y., Zhang, R., Zhang, W., et al. (2017). Crustal deformation in the India-Eurasia collision zone from 25 years of GPS measurements. *Journal of Geophysical Research: Solid Earth*, 122, 9290–9312.